Atmos. Chem. Phys. Discuss., 13, 19751–19835, 2013
www.atmos-chem-phys-discuss.net/13/19751/2013/
doi:10.5194/acpd-13-19751-2013

Atmospheric Chemistry and Physics Discussions

Multi-decadal variations of atmospheric aerosols from 1980 to 2009: sources and regional trends

Mian Chin[1], T. Diehl[1,2], Q. Tan[1,2], J. M. Prospero[3], R. A. Kahn[1], L. A. Remer[4], H. Yu[1,5], A. M. Sayer[1,2], H. Bian[1,4], I. V. Geogdzhayev[6,7], B. N. Holben[1], S. G. Howell[8], B. J. Huebert[8], N. C. Hsu[1], D. Kim[1,2], T. L. Kucsera[1,2], R. C. Levy[1], M. I. Mishchenko[6], X. Pan[1,9], P. K. Quinn[10], G. L. Schuster[11], D. G. Streets[12], S. A. Strode[1,2], O. Torres[1], and X.-P. Zhao[13]

[1]NASA Goddard Space Flight Center, Greenbelt, MD, USA
[2]Universities Space Research Association, Columbia, MD, USA
[3]University of Miami, Miami, FL, USA
[4]University of Maryland, Baltimore County, Baltimore, MD, USA
[5]University of Maryland, College Park, College Park, MD, USA
[6]NASA Goddard Institute for Space Studies, New York, NY, USA
[7]Columbia University, New York, NY, USA
[8]University of Hawaii, Honolulu, HI, USA
[9]Morgan State University, Baltimore, MD, USA
[10]NOAA Pacific Marine Environmental Laboratory, Seattle, WA, USA
[11]NASA Langley Research Center, Hampton, VA, USA

[12]Argonne National Laboratory, Argonne, IL, USA
[13]NOAA National Climatic Data Center, Asheville, NC, USA

Received: 9 July 2013 – Accepted: 12 July 2013 – Published: 26 July 2013

Correspondence to: Mian Chin (mian.chin@nasa.gov)

Published by Copernicus Publications on behalf of the European Geosciences Union.

Abstract

Aerosol variations and trends over different land and ocean regions during 1980–2009 are analyzed with the Goddard Chemistry Aerosol Radiation and Transport (GOCART) model and observations from multiple satellite sensors and ground-based networks. Excluding time periods with large volcanic influences, the tendency of aerosol optical depth (AOD) and surface concentration over polluted land regions is consistent with the anthropogenic emission changes. The largest reduction occurs over Europe, and regions in North America and Russia also exhibit reductions. On the other hand, East Asia and South Asia show AOD increases, although relatively large amount of natural aerosols in Asia makes the total changes less directly connected to the pollutant emission trends. Over major dust source regions, model analysis indicates that the dust emissions over the Sahara and Sahel respond mainly to the near-surface wind speed, but over Central Asia they are largely influenced by ground wetness. The decreasing dust trend in the tropical North Atlantic is most closely associated with the decrease of Sahel dust emission and increase of precipitation over the tropical North Atlantic, likely driven by the sea surface temperature increase. Despite significant regional trends, the model-calculated global annual average AOD shows little changes over land and ocean in the past three decades, because opposite trends in different regions cancel each other in the global average. This highlights the need for regional-scale aerosol assessment, as the global average value conceals regional changes, and thus is not sufficient for assessing changes in aerosol loading.

1 Introduction

Aerosols affect Earth's energy budget by scattering and absorbing solar radiation and by altering cloud properties and lifetimes. They also influence weather, air quality, atmospheric chemistry, and biogeochemical cycles. Anthropogenic activities in the past several decades have caused considerable changes in aerosol composition and loading,

ACPD
13, 19751–19835, 2013

and will continue to do so in the future (e.g., Leibensperger et al., 2012; Sillman et al., 2013). Historic emission inventories have estimated trends in anthropogenic emission closely tied to economic growth, population density, and technological development, which may explain the regional aerosol variability shown in the long-term satellite data records. Furthermore, long-term trends of the observed surface solar radiation have been seen to generally mirror the aerosol emission trends (e.g., Streets et al., 2006), implying a link between aerosol forcing and solar "dimming" and "brightening". Understanding the cause of aerosol changes or trends in terms of human activities or natural variability is key to projecting the Earth system's response to future changes.

Satellite observations of global aerosol distributions started over three decades ago with the Total Ozone Mapping Spectrometer (TOMS) and Advanced Very High Resolution Radiometer (AVHRR). Although these instruments were not specifically designed to measure aerosols, thus having limited accuracy and retrievable information, they provide a long-term perspective on changes over different regions in the world. More recent satellite sensors, such as the Sea-viewing Wide Field-of-view Sensor (SeaWiFS), the Moderate Resolution Imaging and Spectroradiometer (MODIS), and the Multiangle Imaging Spectroradiometer (MISR) instruments included in the Earth Observing System (EOS) satellites have much improved accuracy and enhanced capability in retrieving aerosol amounts, distributions, and physical/optical properties. Although the EOS data period is not long enough to derive multi-decadal trends, they can be compared with AVHRR and TOMS for the overlapping time periods to assess their consistency. At this time, however, it is still difficult to determine unambiguously the origin and composition of aerosols from satellite data alone.

Complementing global satellite observations are several ground-based networks monitoring the changes of aerosols in the past decades. They include aerosol optical depth (AOD) measurements from the world-wide Aerosol Robotic Network (AERONET, Holben et al., 1998, 2001) and surface concentration measurements of aerosol species from several organized/coordinated networks, such as the Interagency Monitoring of Protected Visual Environments (IMPROVE, Malm et al., 1994, 2003) over the United

ACPD
13, 19751–19835, 2013

States, the co-operative program for monitoring and evaluating the long-range transmissions of air pollutants in Europe (EMEP) network over Europe (http://www.emep.int/), the University of Miami managed sites over several oceanic islands (e.g., Prospero, 1999, 2003; Prospero and Lamb, 2003; Savoie et al., 2002), and the sites in the Arctic (Quinn et al., 2007, 2008) used in the Arctic Monitoring and Assessment Program. Although spatial and/or temporal coverage of these data are limited, they provide more detailed information on aerosol properties, long-term variations, and/or measurement accuracy for satellite and model validation.

There have been numerous studies assessing aerosol trends over various spatial domains and time periods. For example, Luo et al. (2001) estimated AOD changes based on the solar radiation data over 46 stations in China and found a significant AOD increase from 1976 to 1990. Massie et al. (2004) used the wintertime TOMS AOD over Asia as a proxy for anthropogenic AOD and found a 17 % increase per decade between 1979 and 2000 over the coastal plains in China and the Ganges river basin in India. The analyses of MISR (Dey and Di Girolamo, 2011), MODIS (Ramachandran et al., 2012) and surface network data (Moorthy et al., 2012) over India showed a statistically significant increase in AOD over many locations between 2000 and 2009, attributed mostly to the increase of anthropogenic aerosols. In contrast, global model simulations (Leibensperger et al., 2012) and IMPROVE measurements over the US (Murphy et al., 2011; Coen et al., 2013) demonstrated a decreasing trend in aerosol concentrations, extinction, and wet deposition fluxes from 1990 to the 2000s. A similar decrease in AOD was also found over Europe from late 1980s to late 2000s from model simulations and measurements (Chiacchio et al., 2011), although the decrease seemed to have occurred mostly during the first half of that period, as surface data from the mid-1990s to 2010 over Europe revealed very little change (Coen et al., 2013). Meanwhile, a decrease of sulfate concentration measured at a site in Israel from the 1980s into the 2000s was linked to the decreasing sulfur emissions in Eastern Europe (Karnieli et al., 2009). Global analysis of satellite data from SeaWiFS between 1997 and 2010 (Hsu et al., 2012) showed a large upward trend in AOD over the Arabian Peninsula, an

ACPD
13, 19751–19835, 2013

increase over China and India, but a decrease over the US and Europe from the 13 yr SeaWiFS observations. Surface sulfate aerosol concentrations over the Arctic have also experienced decreases, with different magnitudes depending on location and time period (Quinn et al., 2007). The changes over ocean, however, are less clear, and different satellite products do not seem to converge on the direction of changes in the past decade (Mishchenko et al., 2007, 2012; Remer et al., 2008; Yu et al., 2009; Thomas et al., 2010; Zhang and Reid, 2010; Hsu et al., 2012; Zhao et al., 2008, 2013), although the "bias-corrected" MODIS and MISR data, that went through additional procedures of removing cloud contamination and correcting wind or microphysical effects on AOD retrieval, showed a statistically negligible global-average trend over ocean from 2000 to 2009, and regional trends similar to those obtained from ground-based measurements (Zhang and Reid, 2010).

Through a global model simulation and analysis of satellite and surface measurement data, this study provides an assessment of aerosol variations and trends over different land and ocean regions over the last three decades (1980–2009) to determine the anthropogenic and natural contributions to these changes. We use the Goddard Chemistry Aerosol Radiation and Transport (GOCART) model, which has incorporated aerosol and precursor emissions from fossil fuel/biofuel combustions, biomass burning, and natural sources (from volcanoes, deserts, and ocean) and is driven by the reanalysis meteorological fields, to simulate the aerosol distributions and tendencies from 1980 to 2009. We consider fifteen land and twelve ocean regions in our analysis (regional domains shown in Fig. 1 and region names and surface areas are listed in Table 1). The land regions are defined mostly according to the geopolitical boundaries of countries or regions, with aerosol source type considerations, to better connect economic development, environmental policies, and aerosol amount within those areas. In the following sections, we first describe the GOCART model simulations (Sect. 2) and the long-term observations used in this study (Sect. 3); we then compare model results of AOD and aerosol concentrations with satellite and surface-based measure-

ACPD
13, 19751–19835, 2013

ments (Sect. 4). We analyze the multi-decadal variations in terms of anthropogenic and natural sources and climate variability (Sect. 5), followed by the conclusions (Sect. 6).

This is the first part of our analysis of long-term aerosol variations and their environmental effects. It also serves as an introduction and background for our other manuscripts currently under preparation that address aerosol effects on surface radiation and source–receptor relationships.

2 Simulations of aerosols with the GOCART model

2.1 GOCART model

Details of the GOCART model are described in our previous publications (e.g., Chin et al., 2000, 2002, 2007, 2009; Ginoux et al., 2001, 2004). Here, we provide a brief summary and describe recent updates. For the present work, the meteorological fields from the Modern-Era Retrospective Analysis for Research and Applications (MERRA) (Rienecker et al., 2011), produced with version 5 of the Goddard Earth Observing System Data Assimilation System (GEOS5-DAS), are used with a GOCART configuration at a horizontal resolution of 2.5° longitude by 2° latitude and 72 vertical levels from the surface to 0.01 hPa. Aerosol simulations in GOCART include the major aerosol types of sulfate, dust, black carbon (BC), organic matter (OM) (or organic carbon OC, typically OM = OC $\cdot f$ where f = 1.4 to 2.2), and sea-salt, and the precursor gas species of SO_2 and dimethyl sulfide (DMS). It also contains another natural aerosols specie, methanesulfonate (MSA, also known as methanesulfonic acid), which is formed from a branch of DMS atmospheric oxidation. The model accounts for emissions from fossil fuel and biofuel combustion, biomass burning, volcanic eruptions, vegetation, deserts, and oceans, and simulates atmospheric processing of aerosols including chemistry, convection, advection, boundary layer mixing, dry and wet deposition, and gravitational settling. The model uses the prescribed oxidant fields of OH, H_2O_2, and NO_3 for sulfur chemistry that are produced from Goddard Chemistry Climate Model (CCM) (Oman

ACPD
13, 19751–19835, 2013

et al., 2011) simulations conducted as part of the Atmospheric Chemistry and Climate Model Intercomparison Project (ACCMIP) project (Lamarque et al., 2013). Aerosol particle sizes from 0.01 to 10 µm are included with parameterized hygroscopic growth, which depends on the ambient relative humidity (RH) and aerosol type. Aerosol extinction is calculated as the product of dry aerosol mass and the mass extinction efficiency of each species; the latter is calculated as a function of particle refractive index, size distribution, density, and ambient RH. A recent update includes dust optical properties that are calculated with the T-matrix code (Dubovik et al., 2006) to account for the non-spherical shape of dust particles (Mishchenko et al., 1997). With the same dust refractive indices (Hess et al., 1998), the T-Matrix calculation of spheroid dust particle shape has shown an increase of dust scattering efficiency by up to10 % at 550 nm, and a much stronger decrease of back scattering efficiency by a factor of about 2.5 compared to Mie calculations for spherical particles (Chin et al., 2002, 2009; Yu et al., 2010).

2.2 Emissions from 1980 to 2009

Emissions of SO_2, BC, and OC from fossil fuel and biofuel combustions and biomass burning are taken from the emission dataset A2-ACCMIP (Diehl et al., 2012), which is one of the multi-year emission datasets available from the international initiative AeroCom project (http://aerocom.met.no) for its second phase (A2) hindcast model experiments. Fossil fuel/biofuel combustion emissions in A2-ACCMIP are from a combination of the historic emissions developed for ACCMIP (Lamarque et al., 2010) for the time period of 1980–2000 and the emission projection from the Representative Concentration Pathways Scenario 8.5 (RCP8.5) (Riahi et al., 2011) after 2000. Annual anthropogenic emissions are generated by linear interpolation of the original ACCMIP and RCP8.5 emissions that were given in decadal increments (plus year 2005 in RCP8.5) (Diehl et al., 2012). The A2-ACCMIP biomass burning emissions from 1980 to 2008 are presented in Granier et al. (2011) as a part of the MACCity (Monitoring Atmospheric Composition & Climate/Megacity-Zoom for the Environment) project. They were gen-

ACPD
13, 19751–19835, 2013

erated by integrating the monthly emissions from the Reanalysis of the Tropospheric Chemical Composition (RETRO, Schultz et al., 2008) between 1980 and 1996 and the Global Fire Emission Dataset Version 2 (GFED v2) (van der Werf et al., 2006) between 1997 and 2008. Biomass burning emission after 2008 is from a linear interpolation of the RCP8.5 dataset (details of A2-ACCMIP dataset can be found in Diehl et al., 2012 and references therein). Unlike our previous simulations of biomass burning emissions when we applied vegetation type-independent emission factors to dry mass burned to estimate tracer emissions from biomass burning (e.g., Chin et al., 2009), here we use the species emissions provided by A2-ACCMIP based on the emission factors from Andreae and Merlet (2001) and updates (Lamarque et al., 2010), which are typically 30–50 % lower for BC and 0–50 % lower for OC than those used in our previous studies, depending on vegetation type (Petrenko et al., 2012).

Volcanic SO_2 emissions are taken from a recently compiled database that includes emission amounts and plume heights (Diehl et al., 2012). The database considers 1167 active volcanoes during 1979–2009 based on the volcanic activity database from the Smithsonian Institution's Global Volcanism Program (http://www.volcano.si.edu/index.cfm), the satellite observations of SO_2 from the Total Ozone Mapping Spectrometer (TOMS) and the Ozone Monitoring Instrument (OMI), and ancillary information from other observations reported in the literature. Global volcanic SO_2 emissions are first calculated based on empirical relationships between the Volcanic Explosivity Index (VEI), the Volcanic Sulfur Index (VSI) and the emission amount (Schnetzler et al., 1997; Chin et al., 2000); such estimates are replaced with available TOMS or OMI observations. Emissions from quasi-continuously erupting (Andres and Kasgnoc, 1998) and silently degassing volcanoes (Berresheim and Jaeschke, 1983; Stoiber et al., 1987) are also included.

Dust emissions are calculated as a function of surface topography, surface bareness, 10 m wind speed, and ground wetness (Ginoux et al., 2001) as follows:

$$E = CSs(r)u_{10\,\mathrm{m}}^2\left(u_{10\,\mathrm{m}}^2 - u_{\mathrm{t}}\right) \quad (1)$$

ACPD
13, 19751–19835, 2013

where E is the dust emission flux, C is a dimensional constant, S is the dust source function (or erodibility) which is a product of the fraction of surface bareness and the topographic depression, $s(r)$ is the fraction of each size class of effective radius r emitted, $u_{10\,m}$ is the 10 m wind velocity, and u_t is the threshold wind velocity which is determined by the particle size and density and ground wetness w. The w also serves as a switch such that dust will only be mobilized when w from the meteorological field (MERRA in this study) is below a threshold value (0.35 in current GOCART). Recently we have incorporated a newly developed dynamic S into the model (Kim et al., 2013). Instead of using the "static" surface bareness from the land cover classification dataset as in previous GOCART simulations, we determine the surface bareness with the 8 km Normalized Difference Vegetation Index (NDVI) data from AVHRR at twice-per-month time resolution (Tucker et al., 2005; Brown et al., 2006) from 1981 to present. NDVI is usually very low when the ground is bare and increases as ground is covered by more vegetation. We choose a threshold NDVI value of 0.15, below which the surface is considered to be bare. The percentage bareness in each model grid cell is determined by the ratio of the number of bare pixels to the total number of 8 km NDVI pixels within the grid cell. This dynamic dust source function considers the seasonal and interannual variations of the surface bareness, which is shown to improve simulated temporal variation of dust aerosols over some semi-arid areas (details in Kim et al., 2013).

Other emissions include oceanic production of sea salt aerosol and DMS and terrestrial biogenic sources of OC that are converted from monoterpene emission. These sources are the same as described in our previous publications (Chin et al., 2002, 2009, and the references therein) with an update of monthly DMS seawater concentrations from a more recent study (Lana et al., 2011). Note that both DMS seawater concentrations and monoterpene emissions are used as "climatology", i.e., inter-annual variability is not considered, even though they provide monthly variations of spatial distributions and intensity.

Figure 2 shows the emissions from fossil fuel/biofuel combustions, biomass burning, and natural sources from 1980 to 2009 used in this study. The land-based emissions

ACPD
13, 19751–19835, 2013

(except volcanic emission) are divided into 15 regions (domains in Fig. 1) to reveal the regional variability or trends. There are large differences among regions on the absolute amount of emitted materials. Fossil fuel and biofuel sources of SO_2 in Canada (CAN), USA, Europe (EUR), and Russia (RUS) decreased significantly from the 1980s to the 2000s; for example, SO_2 emissions in the late 2000s are only about 50 %, 40 %, 20 %, and 55 % of that in 1980 over these regions, respectively, although the decrease is not always monotonic. In contrast, SO_2 emissions in South Asia (SAS), East Asia (EAS), and Southeast Asia (SEA) show the opposite trend as the emissions have increased significantly from 1980 to 2009, by a factor of two in EAS and SEA and by more than a factor of four in SAS. Emissions of carbonaceous aerosols (BC+OC) from fuel combustion sources show similar regional tendencies, although the magnitude of change is smaller than for SO_2 emissions. Biomass burning emissions, on the other hand, demonstrate considerable inter-annual and regional variability (e.g., very high emission in Indonesia in 1997, large boreal fires in Canada and Russia in 1998 and Russia in 2003). Dust and sea salt emissions also vary year-to-year, mainly driven by the 10 m wind speeds and to a lesser extent by the ground wetness for dust emission. The strongest volcanic emission within the 30 yr period is clearly from the eruption of Mt. Pinatubo (located in the Philippines) in 1991, which injected about 20 Tg (10^{12} g) SO_2 into the stratosphere (e.g., Bluth et al., 1992; McCormick et al., 1995). Other significant volcanic eruptions during this period include El Chichón (in Mexico) in 1982 and Miyakajima (in Japan), which erupted in summer 2000 and continued for a few years.

2.3 Model simulations

Using the model configurations and emissions described in Sects. 2.1 and 2.2, we conducted two 30 yr GOCART simulations from 1980 to 2009 (with 6 month spin up): a "standard" simulation that includes all emissions of aerosols and precursor gases, and a "natural" simulation that considers only emissions from natural sources, i.e., deserts, oceans, vegetation, and volcanoes. The differences between the standard and natural

ACPD
13, 19751–19835, 2013

runs are attributed to the contributions from fossil fuel/biofuel combustion and biomass burning sources. We refer these sources collectively as "combustion" sources, which are mostly of anthropogenic origin (although a fraction of biomass burning is natural, i.e., triggered by lightning, especially in boreal regions). These model experiments are used to assess the composition and origin of aerosols and their change over the 30 yr period covered by this study.

3 Long-term observations of aerosols

Aerosol data products from remote sensing and in-situ measurements, together with associated time periods and measured quantities used in this study are listed in Table 2. Figure 3 displays the locations of ground-based network sites, AERONET in Fig. 3a and surface concentration sites (in IMPROVE, EMEP, and University of Miami networks and the Arctic) in Fig. 3b. All data used in this study are monthly averages with the AOD data at 550 nm (TOMS at 500 nm). The satellite data are the gridded (i.e., "level 3") products at $1^{\circ} \times 1^{\circ}$ resolution. Brief descriptions of each dataset are given below.

3.1 AOD from satellite retrievals

Satellite remote sensing of aerosols started more than three decades ago with the TOMS (Hsu et al., 1996; Herman et al., 1997; Torres et al., 1998, 2002) and AVHRR instruments (Stowe et al., 1997; Husar et al., 1997). Despite limitations in accuracy and retrievable information, these observations provide a long-term perspective on regional aerosol changes over global scales. Several retrieval algorithms have been used to extract AOD from the AVHRR-measured radiation reflected by the atmosphere–surface system (e.g., Stowe et al., 1997; Nakajima and Higurashi, 1998; Mishchenko et al., 1999, 2007, 2012; Zhao et al., 2008, 2012). In this study, we use two AVHRR AOD datasets, one produced by the NOAA Climate Data Record (CDR) project (Chan et al.,

ACPD
13, 19751–19835, 2013

2013; Zhao et al., 2013; referred to as AVHRR-CDR hereafter) and the other from the Global Aerosol Climatology Project (GACP, Mishchenko et al., 2012, referred to as AVHRR-GACP hereafter), for their improved accuracy over the earlier operational products due to calibration adjustments and retrieval algorithms upgrades. Because of the relatively bright and highly variable land surface reflectance at the visible wavelengths, the AVHRR retrievals have so far been mostly restricted to oceans (e.g., Stowe et al., 1997). On the other hand, the TOMS aerosol product covers both land and ocean due to its UV wavelength detection capability, for which the surface signal at the top of the atmosphere is usually small. However, because of the coarse instrument spatial resolution (~ 50 km pixel size at nadir), removing cloud contamination for TOMS aerosol retrievals is difficult, which has hampered both the aerosol retrieval availability and data quality, so the uncertainties associated with the TOMS AOD products are relatively large (normally about 30 % over land but worse over ocean; see Torres et al., 2002, 2005).

More recent satellite sensors on board of a series of NASA's Earth Observing System (EOS) satellites, launched in late 1990s or early 2000s (Table 2), have much improved accuracy and enhanced capability for retrieving aerosol amount, distribution, and physical/optical properties, allowing more reliable assessments of aerosol changes, albeit over a relatively short observation period. They include the SeaWiFS (McLain et al., 1998; Hsu et al., 2004, 2012; Sayer et al., 2012), MODIS on the EOS-Terra and -Aqua satellites (Kaufman et al., 1997; Tanré et al., 1997; Remer et al., 2005; Levy et al., 2010, 2013), and MISR on the EOS-Terra satellite (Kahn et al., 2009, 2010), with aerosol products covering both land and ocean. The MODIS AOD product used here is from a combination of the "dark target" retrieval (collection 5), which provides global AOD coverage except over bright desert surfaces (Levy et al., 2010) and the "deep blue" retrieval, which uses the 412 nm channel of MODIS to enable the retrieval of AOD over bright surfaces over land (Hsu et al., 2004).

The monthly average, gridded satellite products are further averaged to yield annual mean values for regional trend analysis. Note that because of the differences in instru-

ACPD
13, 19751–19835, 2013

ment capabilities and swath widths, the spatial and temporal coverage of the data for calculating monthly average can be quite different among the satellite products. For example, MISR's relatively narrow swath (380 km) limits its global coverage to every 9 days at the equator and every 4–5 days at 60° latitude (although its multi-angle capability does capture over-ocean areas that are in sun glint for single-view instruments), whereas MODIS, with its 6 times wider swath (2330 km), provides near daily coverage (although still gaps at the equator and sun glint areas over ocean); TOMS has more missing data in partially cloudy scenes than higher resolution instruments due to its larger pixel size. In addition, at high latitudes, the annual mean values of satellite products are biased toward summer months because of the lengthy darkness in the winter months prohibiting AOD retrieval at UV and visible wavelengths.

3.2 AOD from AERONET measurements

The AERONET program is a worldwide ground-based sun photometer network (Holben et al., 1998, 2001) that started in the 1990s with about a dozen sites and has since grown to include over 200 sites (http://aeronet.gsfc.nasa.gov). The automatic tracking sun and sky scanning radiometers make direct measurements of AOD at several "standard" wavelengths from the near ultraviolet to near infrared during daytime, with an accuracy of ~ 0.01–0.02 (Eck et al., 1999). Because of more direct measurements and unified high standard for instrument calibration, AERONET AOD data are considered as "ground truth" and are widely used for validating satellite products and evaluating model simulations. We use the AOD at 550 nm for comparisons with the satellite data and model output at the same wavelength, which is interpolated from the measured AOD at 440 and 675 nm assuming a linear logarithmic relationship between the wavelength and AOD (i.e., Ångström Exponent). It should be noted that most AERONET sites started AOD measurements in the 2000s and many sites have only short periods of data coverage (e.g., as a part of field experiments); only a few sites provide continuous records covering the past two decades.

ACPD
13, 19751–19835, 2013

3.3 Surface concentration measurements

Over the past two to three decades, several surface measurement networks were established to continuously monitor aerosol and precursor concentrations. However, monitoring networks over land are mostly located in North America and Europe; there are essentially no long-term aerosol concentration measurement networks or monitoring sites in developing countries. In this study we use the surface measurements from several networks/programs and some individual sites: (1) the Interagency Monitoring of Protected Visual Environments (IMPROVE, Malm et al., 1994, 2003) network over the US, which routinely measures aerosol chemical compositions and aerosol extinction at the surface, mostly in national park areas; (2) the Co-operative program for monitoring and evaluating the long-range transmissions of air pollutants in Europe (EMEP) network over Europe, which collects aerosol data in Europe but most long-term data are limited to the "acidifying" (e.g., sulfur) species; (3) the University of Miami-operated network over several islands in Pacific, Atlantic, and Southern Ocean locations, mostly from the 1980s to 1990s and a few lasting into the 2000s (e.g., Prospero et al., 1999; Maring et al., 2000; Savoie et al., 2002), and (4) measurements in the Arctic that were used for assessing the Arctic environment (Quinn et al., 2007, 2008; Arctic Monitoring and Assessment Program, http://www.amap.no) with long-term data mostly limited to inorganic species such as sulfate, nitrate, and ammonia (Quinn et al., 2007 and references therein). A 20 yr measurement record for sulfur aerosol species at Mauna Loa by the University of Hawaii is also use in this study. All data are monthly averages.

4 Multi-decadal variations of AOD over land and ocean regions

4.1 Global AOD distributions

Global distributions of annual averaged AOD at 550 nm for 2001 from AVHRR-CDR, AVHRR-GACP, TOMS, SeaWiFS, MODIS-Terra, and MISR are displayed in Fig. 4, to-

ACPD
13, 19751–19835, 2013

gether with the same quantity simulated with GOCART. All satellite products show that over land, the highest annual averaged AOD values are over dust regions of Sahara desert in Northern Africa, Arabian, Kara-Kum, and Thar deserts in Western and Central Asia, Taklimakan desert in Western China, pollution source regions of Eastern China and India, and biomass burning regions of sub-Sahel and Southern Africa. Among the major pollution source regions, AOD over North America and Europe are significantly lower than that over East Asia and South Asia. Interestingly, TOMS and MODIS show higher AOD in Western US than in Eastern US, whereas SeaWiFS and MISR display the opposite. The MODIS dark target retrieval in the Western US is known to have a high bias because of the relatively high reflective surfaces (e.g., Levy et al., 2010; Chin et al., 2004; Drury et al., 2008), whereas the TOMS retrieval seems to be sensitive to dust and smoke events that occur more frequently in the Western US. Over ocean, satellite data also consistently show elevated AOD in the continental outflow regions, e.g., dust and smoke outflow areas over the Atlantic and pollution/dust outflow areas over the Northern Pacific and Northern Indian oceans. On the other hand, there are clear differences among the satellite products over ocean: on average, the AOD is highest from MISR and the lowest from SeaWiFS; AVHRR-GACP shows the strongest spatial gradient and TOMS shows the weakest due to its poorer detection sensitivity to "background" maritime aerosols (O. Torres, personal communication, 2013); between the two AVHRR retrievals, AOD from CDR is generally lower than that from GACP in mid to high latitudes but is higher in the tropics. There is a distinguishable AOD band in the Southern Ocean centered at about 60° S from AVHRR-GACP, MODIS-Terra, and MISR, which is much less visible from AVHRR-CDR and SeaWiFS (TOMS has very little coverage beyond 45° S). Although a recent study has attributed this AOD band primarily to the contamination by stratocumulus and low broken cumulus clouds in the MODIS retrieval (Toth et al., 2013), the AOD over the Southern Ocean is expected to be higher than that over the tropical remote ocean mainly due mainly to strong winds that drive higher sea salt emissions (see Fig. 2b, last panel and Sect. 4.2.2). Therefore, the band seen in the AVHRR-GACP, MODIS-Terra, and MISR data seems physically

ACPD
13, 19751–19835, 2013

meaningful, although the magnitude is likely biased high because of the cloud contamination and/or other artifacts suggested in recent studies (Zhang and Reid, 2010; Toth et al., 2013; Kalashnikova et al., 2013).

The model captures the high AOD over dust, pollution, and biomass burning regions and the transport of aerosols across the oceans (left panel in the last row in Fig. 4). It also simulates an aerosol band in the Southern Ocean around 60° S, consistent with AVHRR-GACP, MISR, and MODIS, although the magnitude is lower than the satellite retrievals by 0.05 to 0.1, which would be more consistent with the new MODIS product (collection 6; estimated release time in late 2013) with better detection of thin-cirrus clouds and wind-speed correction, resulting in a 0.04–0.12 AOD reduction in the Southern Ocean (Levy et al., 2013). The most significant difference between the model and satellite products appears in the Southern Tropical Oceans where the average AOD from the model is 0.02–0.05, two to five times lower than the satellite retrievals, although the model values are much closer to the AVHRR-GACP than to other satellite products in this region. More quantitative comparisons between the model and satellite data are given in the following section.

The last two panels in Fig. 4 display the geographic distribution of AOD from combustion sources (fossil fuel/biofuel and biomass burning, noted as FF + BB) during 2001 in the model and in the MODIS-based estimate, respectively. The model results are obtained as the difference between the "standard" and "natural" simulations (see Sect. 2.3), and the MODIS-based estimate is derived empirically from the MODIS fine-mode AOD fraction, with corrections to exclude fine mode natural dust and marine aerosols (Kaufman et al., 2005; Yu et al., 2009). The MODIS-based results are only available over ocean because the fine mode fraction over land from MODIS is not reliable. As expected, the model shows that the combustion AOD is mostly concentrated in the pollution and biomass burning source regions over land, but its influence is widespread, extending to the ocean in the Northern Hemisphere and the Arctic, especially over the immediate downwind regions from the continents. The MODIS-based combustion AOD over the ocean shows similar spatial patterns, with higher values over

ACPD
13, 19751–19835, 2013

the continental outflow regions than over the open ocean; but it is higher than the model in the tropical ocean areas around Central America and Indonesia, which may be attributed in part to the volcanic aerosol in these areas (see volcanic emission in Fig. 2b) that is not excluded when deriving the combustion AOD with the Kaufman–Yu empirical method. A relatively high combustion AOD band over Southern Ocean in the MODIS-based product is most likely an artifact.

4.2 Regional AOD trends from satellite data and model

To investigate regional trends, we compare the AOD from satellite retrievals and model simulations over the 15 land and 12 ocean regions (domains in Fig. 1). The Arctic and Antarctic are excluded since little satellite data are available there. The regional average AOD for each dataset is calculated from the available data within the region independently, i.e., spatial and temporal matching of the different datasets and the model is not imposed, not only because there is very limited common coverage, but also because the purpose here is to examine the trends with each dataset independently. Although such averaging can introduce differences between datasets because of the different spatial and/or temporal sampling, the regional trends should be relatively robust, provided the available data are representative.

Figure 5a and b depicts the annual, regional average AOD from 1980 to 2009 from the 15 land and 12 ocean regions, respectively. For each year, model estimated AOD speciation is indicated with color-coded, vertically stacked bars, and the combustion (FF + BB) AOD from the model is shown in red bars next to the aerosol speciation. The only satellite dataset available over land before the EOS era is TOMS; however, as described earlier, it suffers from coarse spatial resolution and the lack of on-board cloud screening capability that limit retrieval availability and data quality. To minimize cloud contamination in the TOMS AOD product, a strict cloud-free pixel standard has been applied that excludes pixels having reflectance exceeding a threshold value. This method unfortunately also removes high-AOD pixels. For example, the large volcanic aerosol signals from El Chichón and Pinatubo are mostly screened out, and the aver-

ACPD
13, 19751–19835, 2013

aged AOD from the remaining pixels is in general significantly lower than the AOD from earlier versions of the TOMS product (e.g., Torres et al., 2002; Chin et al., 2002), by as much as a factor 2–3 in some regions. Because of the TOMS AOD data limitations, they are used mainly for trend assessment rather than for their absolute AOD values, although the TOMS AOD is included in Fig. 5a and b (dash-dotted dark green lines) for informational purposes.

4.2.1 Over land

The model simulation in Fig. 5a shows that the most pronounced feature during the 30 yr time period is the worldwide influence of large volcanic eruptions, i.e., El Chichón in 1982 and Pinatubo in 1991. Sulfate aerosols (thick dark gray bars) formed from these eruptions can last for several years. For the periods lacking major volcanic influences, i.e., in the mid-to-late 1980s and in the 2000s, the model indicates a decreasing AOD trend over wide-spread parts of North America (including CAN, USA, and CAM), Europe (EUR), and Russia (RUS), but an increasing trend over East Asia (EAS), in line with the fossil fuel/biofuel emission changes over these regions (Fig. 2) and also with previous studies (ref. Sect. 1). In Central Asia (CAS), although AOD from combustion sources (red vertical bars) has decreased by 0.04 from 1980 to 2009, dust AOD has increased by 0.04–0.05 over the same time period, offsetting the combustion AOD decrease. The opposite trend is seen from the model simulations for South Asia (SAS), where the combustion aerosol more than doubles between 1980 and 2009 but dust AOD shows an overall decrease by about 30 %, partially masking the combustion AOD increase in the regional average. The model-simulated AOD agrees with the SeaWiFS, MISR, and MODIS data to within 0.05 over CAN, USA, EUR, RUS and EAS but is higher over CAS and lower over CAM and SAS by 0.1–0.2.

Over the major dust source regions of North Africa (Sahara and Sahel, or SHR and SHL) and the Middle East (MDE), AOD from the model tends to be higher than that from the satellite retrievals (other than TOMS) by 0.05 to 0.15, which is likely the results of model overestimating dust emissions. The model shows higher dust inter-annual vari-

ACPD
13, 19751–19835, 2013

ability over the Sahel than Sahara, especially in the early 1980s, reflecting differences between dust emissions in the Sahara and Sahel: although surface wind is the major driver for dust mobilization, changes in vegetation cover and precipitation play additional roles in regulating dust emissions in the Sahel, in contrast with the Sahara, which is always bare and dry. The model shows an increase of dust AOD in the Sahara during the mid to late 2000s, in line with SeaWiFS but not with MISR and MODIS, as both show a slight decreasing tendency. Over MDE, both model and satellite data suggest an increasing AOD tendency in the last 10 yr, driven by the increase of dust, which is consistent with the SeaWiFS analysis and AERONET data in that region (Hsu et al., 2012). Possible causes of dust changes are discussed in Sect. 5.2.

For regions that are mainly influenced by biomass burning, i.e., Southeast Asia (SEA), South America (SAM), and the rest of Africa (RAF), the model-simulated AODs are lower than that from satellite retrievals by more than a factor of two (except SeaWiFS over Southern Africa), suggesting that the biomass burning emission used in the model is likely too low over these areas (Petrenko et al., 2012). Such underestimation is also evident in comparisons with AERONET measurements over these regions (see Sect. 4.3 next). Although biomass burning is an important source of aerosols over the African Savanna (rest of Africa, RAF) and Australia–New Zealand (ANZ), its significance is highly dependent on location and season; on an annual and regional average basis the model suggests a higher dust AOD than biomass burning over these regions, although in RAF the dust influence is mostly confined to north of the Equator (last panel in Fig. 4).

The AOD products from the EOS-satellite sensors (SeaWiFS, MISR, MODIS-Terra and -Aqua) agree with each other in most regions with a few exceptions. Over CAS, EAS, and SAS, AOD from the twin MODIS instrument (Terra and Aqua) is consistently higher than that from SeaWiFS and MISR by 0.05–0.1; AOD from SeaWiFS is lower than that from other sensors over ANZ by 0.03–0.04; and, as mentioned earlier, SeaWiFS shows a different AOD tendency over SHR from MODIS and MISR. Also notice the AODs from the two MODIS instrument – their difference increases over time, with

ACPD
13, 19751–19835, 2013

a noticeable offset in 2009 over SEA, SHL, SAM, and ANZ. This is because of the calibration drift of MODIS-Terra, a problem that is being corrected in the next version (collection 6; Levy et al., 2013).

4.2.2 Over ocean

Over all ocean regions (Fig. 5b), sulfate aerosols from the El Chichón and Pinatubo volcanic eruptions are again the most distinct features in the long-term record from both AVHRR retrievals and GOCART simulations. The AVHRR data show comparable maximum AOD values between El Chichón and Pinatubo over the northern hemispheric oceans, whereas GOCART generates a higher AOD from Pinatubo than from El Chichón over every oceanic region. In the time periods with little influence from major volcanic eruptions, GOCART matches the two AVHRR and SeaWiFS retrievals within 0.02–0.03 in the 30° N–66.5° N oceanic regions of the North Atlantic (NAT) and Western and Eastern North Pacific (WNP and ENP) (panels 1–3 in Fig. 5b), although it is about 0.02–0.08 lower than MISR and MODIS in the same regions. In the eight tropical/subtropical regions between 30° N–45° S (panel 4–11), the model is consistently lower than all satellite products except over the African dust outflow region (CAT) before 2000. The differences between GOCART and satellite AOD over the tropical/subtropical oceans fall generally within 0.05–0.1. In the Southern Ocean (SOU) between 45° S and 66.5° S, AOD values from GOCART, AVHRR-CDR, and SeaWiFS are close to each other, but they are much lower than other satellite products. As noted earlier (Sect. 4.1), further corrections of thin-cirrus cloud and wind speed would bring the MODIS AOD down by 0.04–0.12 in this region (Levy et al., 2013).

The large underestimation of AOD by the model over much of the tropical and subtropical ocean suggests that the model may have missed some aerosol sources over these remote ocean regions. Recent studies have suggested incorporating a temperature-dependent sea salt emission scheme that would increase the sea salt emissions in low latitudes (Jaeglé et al., 2011) and improve the agreement with the satellite data, or considering primary organic matter emissions over oceans (Gantt

ACPD
13, 19751–19835, 2013

et al., 2011). On the other hand, satellite AOD may exhibit a high bias over the ocean, which could be caused by contributions from unscreened cloud or unaccounted-for whitecaps (e.g., Mishchenko et al., 1999; Kahn et al., 2007). For example, after applying extensive quality assuring procedures (including removal of possible cloud contamination, corrections for wind speed, and corrections of fine mode fraction), the improved AOD from MODIS over ocean is 0.05–0.15 lower than the standard MODIS products (Zhang and Reid, 2006, 2010), and a study comparing AOD from MODIS, MISR, and several global models against the measurements on shipboard from the AERONET Maritime Aerosol Network (MAN) reveals a general high bias of the standard MISR and MODIS AOD data over the ocean (Smirnov et al., 2011). The latter study also showed a 0.02 low bias of AOD in the Southern Hemisphere tropical ocean and a 0.02 to 0.05 high bias over mid-latitudes for a previous version of GOCART.

Interestingly, the AOD composition from GOCART indicates that sea salt is not the major components for maritime aerosol even during the time periods without El Chichón or Pinatubo influences, except in the Southern Ocean. Pollution and dust transport constitute more than half of the AOD over the northern hemispheric ocean regions in mid-latitudes and Indian Ocean, whereas biomass burning and natural aerosols (volcanic, DMS oxidation) influence the AOD in the tropical and subtropical areas. A study of MODIS fine-mode aerosol data over ocean (Yu et al., 2009) argues that the sulfate contribution via DMS-SO_2 oxidation could be higher than previously thought in tropical and some mid-latitude regions, producing large seasonal and geographical variations of fine-mode fraction of AOD for marine aerosols that would be consistent with observations (Wilson and Forgan, 2002; Shinozuka et al., 2004; Yu et al., 2009). Over the remote areas (ECP, WSP, ESP, and SOU) with low anthropogenic or dust influences, the model indicates a predominance of natural sulfate over the Pacific regions (ECP, WSP, and ESP), although the sea salt contribution may be underestimated without the sea surface temperature adjustment (Jaeglé et al., 2011). In contrast, AOD over SOU (panel 12 in Fig. 5b) is higher than that over other remote ocean regions (ECP, WSP, and ESP) mainly because of the higher sea salt amount generated by stronger

ACPD
13, 19751–19835, 2013

winds. The model suggested that about 20–25 % of AOD over SOU is contributed by sulfate formed via DMS-SO_2 oxidation (indicated by SU in SOU region in time periods without large volcanic influences), which was also shown in our previous model studies (Chin et al., 2002, 2009).

The most clear regional changes over ocean from the mid 1980s to 2000s are the declining trends over NAT and CAT, thanks to the reduction of anthropogenic and dust influences from the neighboring continents. Similar to the change in SAS, the model suggests that the increase of anthropogenic AOD over the North Indian Ocean (NIN) is damped by a decrease in dust AOD. In the most recent decade, MISR suggests a decrease of AOD over most of these regions, whereas the other satellites show little change or slightly increasing trends. The overall inter-decadal changes will be discussed in the subsection below.

Despite considerable similarities among satellite AOD products, there are noticeable differences as well. Between the two AVHRR retrievals, for instance, AOD from GACP is about 0.1 higher than that from CDR in the Southern Ocean in most years. The spatial coverage can also be different between the two products due to differences in cloud screening and retrieval availability from their respective calibrations (Li et al., 2009); such differences can contribute to discrepancies in the annual and regional averaged values. There is an abrupt increase of AOD in the CDR product in 1995–1997 over the tropical and subtropical regions that does not appear in the GACP data. The CDR data also show an AOD peak in 2007 over most of the tropical/subtropical regions that does not seem to be consistent with other satellite products. The year-to-year variabilities among the more recent SeaWiFS, MISR, MODIS-Terra, and MODIS-Aqua satellite products closely track each other, but the AOD from MISR is consistently highest and SeaWiFS is lowest over the ocean (also see Fig. 4), with the difference between 0.01 to 0.08, a discrepancy that is generally consistent with previously reported results of 0.025 high bias from MISR (e.g., Kahn et al., 2010; Smirnov et al., 2011) and 0.01–0.015 low bias from SeaWiFS over the ocean (Sayer et al., 2012).

ACPD
13, 19751–19835, 2013

4.2.3 Global patterns of AOD change

Because significant perturbations from sporadic events, mainly large volcanic eruptions, skew otherwise rather smooth changes, it is difficult to deduce a linear trend from the 30 yr AOD record. It is also not assured that AOD changes over 30 yr would be linear, or even monotonic, in all regions. Instead, we examine the differences between the beginning and end of two time segments, (1) the end of 1980s (1988–1989) to early 2000s (2000–2001), and (2) the early 2000s (2000–2001) to the end of 2000s (2008–2009), to reveal the geographic pattern of AOD changes during these two periods. The time segments were chosen to minimize large volcanic influences, to maintain close to normal climate conditions (i.e., near neutral El Niño-Southern Oscillation index after averaging over two years), and to optimize the use of multiple satellite datasets that cover different time periods (see Table 1). In the first time segment, available satellite data include AVHRR-CDR, AVHRR-GACP, and TOMS whereas in the second time segment AVHRR-CDR, SeaWiFS, MODIS-Terra, and MISR are available. AVHRR-CDR is the only satellite dataset that provides three decades (1981–2009) of coverage. The difference maps are shown in Fig. 6a and b, respectively, for the two time segments. Although a two-year period seems relatively short for averaging, and the difference between the beginning and end of a time segment could reflect inter-annual variability rather than the decadal trend, such spatial difference maps together with the regional time series in Fig. 5 do provide useful information about decadal-scale variations.

During the first time segment (Fig. 6a), both AVHRR products (first two panels in the left column) indicate a widespread AOD decrease over the ocean from the end of the 1980s (1988–1989) to the beginning of the current century (2000–2001), except in coastal areas of the Indian Subcontinent, North Pacific mid-latitudes, and tropical African west coast. The GACP product also shows pockets of increase over the Southern Ocean. In contrast, TOMS (bottom panel, left column) presents a general AOD increase over large oceanic area, except some areas over the Atlantic. However, the increase (0.02–0.05) is well within the range of the relatively large uncertainties

ACPD
13, 19751–19835, 2013

in TOMS AOD (see Sect. 3.1), hence the apparent trend is not conclusive. All satellite products show a clear AOD decrease off the west coast of North Africa and Angola but an increase in the tropics at latitudes between these two coastal areas. The AOD changes near the coastal regions usually reflect directly the changes of aerosol sources in the upwind land regions. For example, the TOMS shows an AOD increase over Asia and Southern Africa, a decrease over Russia and Europe, and a strong decrease over Northern Africa and Brazil. Over North America, TOMS shows an increase in the Western US, with "hot spots" on the north and south borders possibly because of the difference in biomass burning between 2000–2001 and 1988–1989, and some decreasing tendency in the Eastern US and Southern Mexico.

In comparison, the total AOD change from GOCART during the first time segment (Fig. 6a, top right) is generally smaller (ΔAOD within ±0.02) than that from satellite data over the ocean. Qualitatively, GOCART is consistent with the data showing a decrease over the North Atlantic in mid-to-high latitudes (> 30° N) and subtropical areas off the west coast of Northern Africa, and increases along the coast of Central Africa, the Northern Indian Ocean, and Western North Pacific. Over land, the model shows a 0.1–0.2 AOD decrease over most of Europe, a 0.05–0.1 decrease over Russia and Northern Africa, and smaller decreases over Canada, Eastern US, and parts of South America and Australia. Increases appear over Central and Eastern Africa, the Middle East, Central Asia, and East and South Asia. The direction of these changes is generally consistent with the TOMS data with a few exceptions (e.g., Australia, Patagonia, and Europe, where TOMS has little coverage), although the magnitude is smaller. The model also displays a 0.05–0.1 AOD decrease over the Arctic, where no satellite data are available. From the simulation separating natural from FF + BB burning emissions (middle and lower panels in the right column of Fig. 6a), the model reveals that the changes over North America, Europe, Russia, South Asia, East Asia, and the Arctic are mainly because of the combustion (mostly fossil fuel) emission changes; interestingly, as we have seen in Fig. 5a, the changes of dust and combustion AOD are in opposite directions over Central Asia and India. The decrease over Northern Africa and

ACPD
13, 19751–19835, 2013

increase over Central Asia reflect the dust emission changes, whereas the increase in Southern Japan is due to the volcanic activity from Miyakajima which was quite active in 2000–2001 but not in 1988–1989. The AOD increase in Eastern and Central Africa is a combination of stronger dust activity in South Sudan and Central Africa, and larger volcanic emissions in the Congo region in 2000–2001 compared to 1988–1989.

During the second time segment (Fig. 6b), the tendency of AOD change from AVHRR-CDR over the ocean is different from the first one. In contrast with the decreasing AOD trends over large ocean areas during the first time segment, it shows an increasing trend in the range of 0.02 to 0.2 over the tropics and Southern Ocean near Antarctica, and a 0.02–0.05 decrease in the North Atlantic near the coastal regions. All satellite data show an AOD increase over the Northern Indian Ocean, with larger increases from AVHRR-CDR and MODIS-Terra (0.05–0.20) than from SeaWiFS and MISR (0.02–0.10). Over land, the three EOS satellite sensors all show an AOD decrease over the Eastern US, Europe, South America, and Southern Africa but an increase over Eastern China and India, although the magnitudes of the changes are not always the same. Over major dust regions (North Africa, the Middle East, and Central Asia), SeaWiFS and MISR in general show an increase, especially the "hot spot" of 0.1–0.2 AOD increase over the Arabian Peninsula from SeaWiFS, which occurred mostly in spring and summer (Hsu et al., 2012). (Note that there are no MODIS-Terra products available for 2000 over the deserts from the Deep Blue algorithm.)

There are a number of noticeable differences among the satellite datasets: SeaWiFS and MISR show a decrease of dust across the tropical Atlantic that is absent in the AVHRR-CDR and only slightly visible in the MODIS-Terra; AVHRR-CDR and MODIS-Terra display an increase off the west coast of Southern Africa but MISR indicates a decrease; SeaWiFS, MODIS-Terra, and MISR all show an increase over the northern part of North Pacific but AVHRR-CDR does not agree; SeaWiFS, MODIS-Terra, and MISR show an increase in the Arctic ocean but AVHRR shows a decrease in the same region; and MISR displays an average negative trend over ocean but other sensors

ACPD
13, 19751–19835, 2013

seem to have an overall positive trend, albeit most values are within ±0.05, i.e., within the uncertainty range of the sensors.

The model, on the other hand, indicates a smaller AOD change (within ±0.02) than satellite products over most oceanic areas in the last decade, but shows a decrease off the west coast of Northern and Southern Africa that is similar to SeaWiFS and MISR, a decrease over the east coast of North America and west of Central America that is consistent with AVHRR-CDR and MISR, and a decrease in the Northwest Pacific east of Japan, the Arctic Ocean, and the Southern Ocean near Antarctica that are either not evident from the satellite data or not observable by the satellites, possibly due to persistent cloud cover. Over land, the model shows a continuous decrease of AOD over the US, Europe and Russia and a continuous increase over East Asia and part of South Asia from the previous decade (Fig. 6a). Over the desert regions, the model also simulates an increase over North Africa, the Middle East, and Central Asia, in the same direction as the changes seen in SeaWiFS and MISR, although the increase in the Arabian Peninsula (0–0.05) is much weaker than the magnitudes from SeaWiFS (0.1–0.2) and MISR (0.02–0.1). Another intriguing change during the last decade is in the dust source and outflow regions of North Africa and the tropical North Atlantic: The model shows that the AOD over the tropical North Atlantic has been decreasing in both time segments, despite the AOD increase in the upwind North African dust source regions in the second time segment. The model-calculated changes in the latter time segment is supported by the SeaWiFS data and, to some extent, by the MISR data as well. We discuss the controlling factors of dust emission and transport in Sect. 5.2.

Although there are differences in the AOD changes in different satellite products, the data are usually consistent over land as well as the outflow regions over ocean, and can be explained mostly by the changes of land-based emissions. Satellite data have larger relative uncertainties over remote areas because of low AOD, and additional difficulties at high latitudes due to the high reflective surfaces, low sun angle, and persistent cloud cover. Also keep in mind that the earlier TOMS and AVHRR satellite sensors were not designed for aerosol retrieval, so the products are expected to have larger uncertainties

ACPD
13, 19751–19835, 2013

than data from the more recent EOS sensors. In the following sections (4.3 and 4.4), the model simulations are further evaluated with ground-based observations during the past three decades.

4.3 AOD at AERONET sites

We compare the AOD from GOCART simulations with that measured from the worldwide AERONET sites. As we mentioned in Sect. 3.2, only a few AERONET sites existed in the mid 1990s, which limits the use of AERONET data to assess multi-decadal trends. Rather, we use the AERONET data to verify the seasonal and inter-annual AOD variations simulated by GOCART in different regions. The GOCART output and satellite retrieval at each AERONET site are extracted from the data within the grid cell that contains the AERONET site. Comparisons at selected sites are shown in Fig. 7, and the overall statistics is listed in Table 3. The statistic quantities include the correlation coefficient R, the root-mean-square-error E, the mean bias B (defined as the ratio of the model results to the data), and the skill score S (a combined measure of correlation and standard error between observation and model, see Taylor, 2001).

Figure 7 shows the monthly average AOD from 1994 to 2009 from AERONET and GOCART at 14 AERONET sites over continents (Fig. 7a) and 10 sites over oceanic islands (Fig. 7b), one for each land/ocean region shown in Fig. 2 (no AERONET long-term data are available in CAS, WCP, and SIN). These sites were selected for having the longest available data record among all sites within their respective regions. We also include the satellite data in these comparisons for information purpose (except AVHRR as they are only available over ocean). The aerosol composition from GOCART is displayed as vertically stacked color bars. AOD exhibits large seasonal variations that are much stronger than inter-annual variability, especially over the biomass burning sites (i.e., OM dominated sites in Fig. 7). Over land, the model performs best over dust-dominated sites, Saada in the Northern Sahara (Morocco), Banizoumbou in the Sahel (Niger), and Sede Boker in Israel. At the sites heavily influenced by biomass burning (Mukdahan in Southeast Asia, Mongu in Southern Africa, Alta Floresta in South Amer-

ACPD
13, 19751–19835, 2013

ica, and Lake Argyle in Australia), the modeled AOD is 30–60 % lower than AERONET even though the model captures the seasonality. Considering that the model had much smaller bias (within 20 %) in our previous studies using a higher biomass burning emissions (about a factor of 2 higher globally than the A2-ACCMIP, see Chin et al., 2009), we suggest that the biomass burning emissions provided by A2-ACCMIP used here are likely too low (see also Petrenko et al., 2012). For other land regions, the model has most difficulty over Mexico City, where the AOD from the model is only about 40 % of that from AERONET, and Kanpur (India), where the model severely underestimates the wintertime aerosol levels by a factor of 2 to 5. The problem in Mexico City and Kanpur might be associated with the "missing" aerosols in the model (e.g., anthropogenic secondary organic aerosol, nitrates), uncounted emissions, poor representation of meteorological conditions (especially the planetary boundary layer or PBL height and RH), and inadequate model spatial resolution to resolve the complex Northern Indian terrain (e.g., Pan et al., AGU 2012 presentation). Satellite data are generally consistent with the AERONET data at these continental sites in both temporal variation and magnitude, except at Bratts Lake and Sede Boker where most of them are too high, and Mexico City where most of them are too low compared to AERONET. Differences in spatial sampling between the satellite retrievals and AERONET are likely to play a role in the discrepancies.

Much less AERONET data are available from the island sites (Fig. 7b) than from the inland sites. The model represents the observations best at the continental outflow locations (such as Gosan on the route of Asian outflow, San Nicolas near the coast of Southern California, and Cape Verde receiving dust outflow from North Africa) and worst over tropical sites (such as the Maldives Climate Observatory in the North Indian Ocean, Nauru and Tahiti in the remote tropical South Pacific, and Ascension Island in the tropical South Atlantic) where the model underestimates the AOD by a factor of 2–3. Interestingly, most satellite data are higher than AERONET over the remote locations, most likely the result of the low AOD values that are close to or below the

ACPD
13, 19751–19835, 2013

satellite detection limit. Overall statistics of the GOCART-AERONET comparisons are listed in Table 3.

4.4 Surface concentrations

In this section we evaluate model results with long-term surface concentration measurements mostly from several organized/coordinated ground networks described in Sect. 3 (site locations in Fig. 3). Unlike the remotely-sensed AOD data (discussed in the previous sections), which are optical measurements of the atmospheric column and in most cases do not distinguish aerosol species, the ground-based in-situ measurements provide mass concentrations of different aerosol species and their precursor gases, although only at the surface. However, the spatial coverage of the long-term concentration measurements over land is mostly limited to locations in North America and Europe (see Fig. 3). Comparisons at selected sites shown in Fig. 8a–e are given as examples, and the overall statistics is listed in Table 3.

4.4.1 Concentrations at land sites

Over the US: Fig. 8a shows surface concentrations of sulfate, BC (or elemental carbon – EC – in IMPROVE), OC, and fine-mode dust at two IMPROVE sites from 1988 to 2007. One site is located in a relatively remote area in the Southwestern US, San Gorgonio Wilderness (SAGO1) in Southern California at 1.7 km elevation, and the other is located in an urban location of Washington DC (WASH1) in the Eastern US near the sea level. Concentrations of sulfate, BC, and OC over SAGO1 are significantly lower than those over more polluted WASH1 from both model and observations. The model shows about a 30 % reduction of sulfate at both SAGO1 and WASH1 sites over the 20 yr time span, consistent with the IMPROVE observations, although the modeled sulfate is nearly twice as high as observation at SAGO1. The observations also show a 30–40 % reduction of BC and OC at WASH1 for the same period; however the model not only underestimates the amount of BC and OC but also shows smaller changes

ACPD
13, 19751–19835, 2013

during the 20 yr period, driven by the emission changes (Fig. 2). In the Western US, BC and OC do not exhibit significant trends, and the model is again too low, especially for OC. Although the IMPROVE data show similar fine dust amounts at SAGO1 and WASH1 and a small decreasing trend at SAGO1, the model-calculated fine dust at SAGO1 is about twice as high as that at WASH1 because of the proximity of SAGO1 to the local desert in the Southwestern US and more prone to receiving the transpacific transport of dust (Chin et al., 2007), making the model 65 % higher than observations at SAGO1 and 23 % lower at WASH1 with no clear trend at SAGO1.

Over Europe: The long-term measurements of aerosol and related species in the EMEP network sampled the "acidifying" compounds, starting in the late 1970s. Measurements of other species such as BC and OC started much later, mostly in the 2000s. Therefore in this study we use the sulfur data from EMEP. Figure 8b shows the long-term data of SO_2 (a precursor gas for sulfate) and sulfate at two EMEP sites, Schauinsland in Germany and Uto in Finland. There has been a more than 5-fold decrease of SO_2 emissions between 1980 and 2009 in Europe (Fig. 2), leading to a surface SO_2 concentration decrease of the same magnitude. Consequently, the concentration of the SO_2 oxidation product, sulfate, has also significantly declined in the past three decades, though more gradually and by a smaller amount than SO_2. Such reductions are widespread over Europe, and are mostly responsible for the decreased aerosol amount in the Arctic. The model overestimates SO_2 by more than a factor of 2 and sulfate by 60 % at Schauinsland with most of the overestimation before 2000. On average, the modeled SO_2 at all EMEP sites is nearly 90 % higher than observations (Table 3) but the sulfate is only about 20 % higher, mostly because the conversion of SO_2 to sulfate is limited by the availability of the oxidants (OH, H_2O_2) in the polluted regions (Chin et al., 1996, 2000; Koch et al., 1999) such that the excess SO_2 remains in the gas phase.

Over the Arctic: Fig. 8c shows the surface sulfate concentrations at four sites inside the Arctic Circle, two located in the Western Arctic (Barrow, Alaska and Alert, Canada) and two in the Eastern Arctic (Spitsbergen and Karasjok, Norway). The data records

ACPD
13, 19751–19835, 2013

for Barrow and Spitsbergen started in the late and early 1990s, respectively, and are shorter than those for Alert and Karasjok. Because of the remoteness of these sites, sulfate there is mostly transported from the mid latitudes polluted areas, as was first observed in the 1970s (e.g., Shaw and Stamnes, 1980; Rahn, 1981). Sulfate concentrations from both observations and model display a remarkable decrease at Alert and Karasjok starting from the early 1990s and late 1980s, respectively, such that the concentrations in the 2000s are 3–5 fold lower than the earlier values. Model results suggest similar changes at Barrow and Spitsbergen even though no data are available in the 1980s. Such large reductions of sulfate at the Arctic sites are consistent with the comprehensive data analysis on Arctic aerosol composition and trends (e.g., Quinn et al., 2007, 2008). Although located in the Western Arctic, surface concentrations at Alert and Barrow may be influenced more by the transport of pollutants from Europe than from North America, as our previous model study indicated (Chin et al., 2007). The model overestimates sulfate at Spitsbergen by more than 80 % in the 1990s, likely from the excessive sulfate production by transported SO_2 from lower latitudes over Europe where SO_2 is overestimated by the model (see the previous paragraph).

By separating combustion-generated aerosol species from the natural ones (dust, biogenic, and volcanic), the model shows that sulfate over land is mostly from the combustion sources (red dotted lines in Fig. 8). BC is entirely from the combustion sources, whereas a sizable fraction of OM can come from natural sources (biogenic secondary organic aerosol) depending on the locations (such as at WASH1 in Fig. 8a).

4.4.2 Concentrations at oceanic island sites

Surface aerosol concentrations at 15 island sites from the University of Miami network are available between 1981 and 2002, but there are significant data gaps for some species. We show sulfate, dust, and sea salt concentrations at two Northern Hemisphere sites, Barbados in the North Atlantic and Midway Island in the North Pacific (Fig. 8d), and sulfate, sea salt, and MSA at two Southern Hemisphere sites, Norfolk Island in the South Pacific and Mawson Station on the Antarctic coast (Fig. 8e). Note that

ACPD
13, 19751–19835, 2013

the sulfate term used here is for "non-sea-salt-sulfate". Overall, both measurements and model show large seasonal and intra-seasonal variations with no clear trends over the 22 yr period, although sea salt at Barbados seems to have increased from 1985 to 2000 according to the data, but such an apparent increase is attributed to measurement inconsistency during this period (change of sampling height and filter head placement, J. Prospero, personal communication, 2013). Most dust at Barbados is from North Africa and at Midway Island from Asia (e.g., Prospero et al., 1999; Prospero and Lamb, 2003; Chin et al., 2007). The model captures the seasonal variation of dust at both Barbados and Midway but overestimates the amount by a factor of 2 at Barbados and 5 at Midway (Fig. 8d), suggesting that the model may significantly overestimate the dust source strength and/or underestimates the loss during transport from the source regions in Africa and Asia. However, such a conclusion would not be consistent with the comparison with AERONET AOD, where the model-simulated AOD is lower than AERONET by about 75 % at both islands (Midway comparison in Fig. 7b, Barbados comparison not shown for AERONET data only available for two years there). One possible explanation is that the model may have misplaced dust vertical location to have it mostly concentrated near the surface. However, our previous studies on comparisons with the aerosol extinction vertical profiles from the Cloud-Aerosol Lidar with Orthogonal Polarization (CALIOP) in the dust outflow regions of the Western Pacific and the North Atlantic imply the opposite – the dust effective heights from the model is higher than that derived from the CALIOP data (Yu et al., 2010; Koffi et al., 2012). Incorrect dust size distributions or optical properties could be another reason to explain the discrepancy. This is a subject for further investigation.

Natural aerosols constitute a major fraction of aerosols at the locations of Norfolk Island in the Southern Pacific and Mawson on the Antarctic coast (Fig. 8e). The important source of natural sulfate over ocean is the photochemical reactions that oxidize DMS; a branch of DMS oxidation pathway also produces another natural aerosol species, MSA. Both sulfate and MSA at Norfolk and Mawson have strong seasonal cycles with peaks in the Southern Hemisphere summer, reflecting the seasonal cy-

ACPD
13, 19751–19835, 2013

cles of ocean primary productivity and atmospheric photochemical processes, both of which are strongest in the summer. Note that sulfate at Norfolk Island is heavily influenced by volcanic sources on the nearby islands (Diehl et al., 2012), such that the seasonal cycle of sulfate at Norfolk Island is less regular than at Mawson. The seasonal cycle and magnitude of sea salt aerosols, on the other hand, is controlled by the surface wind intensity (e.g., Gong, 2003), which is usually stronger in winter than summer. Therefore, sulfate and sea salt seasonal cycles are expected to have opposite temporal phases. At Mawson, the model agrees with sulfate and MSA observations within 30 % and 18 %, respectively, but its sea salt concentrations are higher by more than a factor of 8, although the sea salt level at Mawson is much lower than at other ocean sites. The large discrepancy of sea salt at Mawson can be attributed mostly to the strong influence of katabatic flow off the inland ice dome (Prospero et al., 1991; Savoie et al., 1992), which prevents sufficient transport of sea salt directly to Mawson by on-shore winds. Such katabatic flow is not resolved in the model. The high degree of agreement between modeled and observed MSA at Norfolk and Mawson suggests that the biogenic sulfur cycle over the regions around the two sites is well represented in the model.

Lastly, the sulfate and MSA measurements at Mauna Loa Observatory (MLO) from 1989 to 2009 by the University of Hawaii and the corresponding model results are shown in Fig. 8f. The model results are closer to the observations in the middle to the end of the 1990s, but for other periods the agreement is worse, especially the modeled sulfate from 2005 to 2009, which is much lower than the measurements. The model produces a sulfate peak in the spring from the transpacific transport, whereas the data show a summer maximum. Compared with the regular, clear seasonal cycles of MSA in Norfolk and Mawson (Fig. 8e), MSA at MLO is much less organized because it is mostly transported from lower altitudes to MLO, which is situated above the PBL at 3.4 km. As the measurements were conducted under selected conditions, such as sampling at nighttime and avoiding local influences, this may contribute to the rather low correlation between the model and data, but it is unlikely to explain the low bias

ACPD
13, 19751–19835, 2013

from the model. The poorer agreement between the model and the MLO data certainly reflects the difficulty of correctly handling the terrain-affected transport with a 2.5° × 2° horizontal resolution model.

Compared to surface sulfate at the land sites that is predominantly from combustion sources, the model reveals that over the ocean sites (Fig. 8d–f) a large fraction of the sulfate is from natural sources (e.g., DMS oxidation, or volcanic SO_2 oxidation). Among the sites shown in Fig. 8d–f, this natural sulfate fraction varies from about half at Barbados and Midway to nearly 90 % at Mawson according to the model.

The statistics of model comparisons with ground-based observations presented in Sects. 4.3 and 4.4 are listed in Table 3. The model performs best in simulations of total-column AOD (AERONET) and surface sulfate concentrations with skill score S above 0.75 (0.75–0.90) and relative bias B within 32 % (0.92–1.32), and worst for OC concentrations in the US, with $S = 0.58$ and $B = 0.56$. The model-simulated surface dust concentrations are 60–97 % too high compared with surface measurements in the US (IMPROVE) and at the ocean islands (Univ. Miami), and SO_2 is almost 90 % higher than the measurements for Europe (EMEP), although the sulfate difference is much smaller (within 22 %) due to the limitation of SO_2-to-sulfate conversion by available oxidants, as discussed previously.

5 Discussion

5.1 Relationships between emission, surface concentration, and AOD in polluted regions

To estimate the effects of changing emissions on AOD and surface concentration, it is necessary to examine the relationships between those quantities in different regions. Yet, many factors other than "domestic" emissions can influence such relationships, such as transport (net import vs. net export), removal efficiency (dry vs. wet regions), source type (surface sources vs. higher-altitude sources), and source density (total

ACPD
13, 19751–19835, 2013

emission per unit area), so that the relationship of emission-AOD-surface concentration can be quite different from region to region, and the regional AOD and/or surface concentrations may not be controlled by or respond linearly to regional emission changes. With that in mind, and meanwhile to shed light on the plausible responses of atmospheric aerosol to regional emission changes within these regions, we simply show the relationships between emissions and model-calculated AOD or surface concentrations within four major anthropogenic source regions: USA, EUR, EAS, and SAS, which are known to be net export regions. More quantitative assessments of local/regional aerosol source attribution sand source–receptor relationships require model experiments that "tag" emissions based on source region and/or type (e.g., Chin et al., 2007; HTAP 2010; Yu et al., 2013), an approach that is not covered here.

We select years that are not influenced by large volcanic eruptions (1980–1981, 1988–1990, 2002–2009) to minimize ambiguities and to concentrate on emissions predominantly within the PBL. We perform a linear fit between the total annual emissions and the annual averaged surface concentration or AOD within each region for sulfur (sulfate AOD, total sulfur emission), OM, and BC, as they are mostly generated from combustion sources. The correlation coefficient indicates how closely the concentrations or AOD reflect the regional emission, and the slope may suggest the change of concentration or AOD per unit change of regional emission. The results are shown in Fig. 9.

The emissions and surface concentrations in these regions exhibit a tight linear relationship on a regional and annual average basis, with correlation coefficients above 0.9 for all regions and all species except OM in East Asia, where $R = 0.85$. This relatively low correlation is attributable to one outlier of OM concentration at nearly 6 $\mu g\,m^{-3}$ in 2003, mostly due to OM imported from large boreal fires in Eastern Russia during the spring and summer that year (Edwards et al., 2004; Generoso et al., 2007). The high correlations between emissions and surface concentrations of all species strongly imply that overall, the air quality in those regions with respect to particulate pollution

ACPD
13, 19751–19835, 2013

is mainly controlled by emissions within the region, as suggested by several previous studies (e.g., Chin et al., 2007; HTAP 2010).

In contrast, emissions and AOD are not as closely related, even though in Europe and South Asia the correlation coefficients are still high, in the range of 0.94 to 0.99. The looser correlations between regional emissions and AOD imply that long-range transport from extra-regional sources can be significant, as transported aerosol usually has a larger influence aloft than at the surface over receptor regions (e.g., Chin et al., 2007; Yu et al., 2012, 2013). For example, the correlation coefficients between emissions and AOD for OM and BC over the US are 0.65 and 0.78, respectively, significantly lower than the 0.93 and 0.99 between emissions and surface concentrations. A previous modeling study estimated that BC from Asia could contribute up to 50 % of total BC at 2 km and an even higher percentage at higher elevation in spring (April 2004) off the west coast of North America (Hadley et al., 2007), although at higher altitudes BC concentrations are usually much lower than in the boundary layer. Another recent study found that intercontinental transport contributes about 28 % of BC AOD and 21 % of OM AOD over North America, averaged over 9 global models, that is dominated by the emissions from East Asia (Yu et al., 2013). Surprisingly, the weakest correlation between emissions and AOD from the model is with sulfur over East Asia ($R = 0.53$ between SO_2 emission and sulfate AOD), a region that is known to be a major anthropogenic SO_2 source and net exporter of pollutants, especially in the recent decade, so a high correlation is expected. By examining the anthropogenic and natural components of sulfate AOD from regional and extra-regional sources, we find that natural volcanic aerosols play an important role in shifting the expected sulfur emission and AOD correlation in the model. There have been numerous active volcanoes in the Kamchatka Peninsula (Russian Territory, outside the EAS domain) that frequently release SO_2 into the atmosphere. These emissions can inject SO_2 to high altitudes, producing large spatial and temporal-scale influences. For example, the 1981 Alaid volcano eruption was one of the largest on record in the Kuril Islands (just south of Kamchatka), injecting about 1100 kilotons of SO_2 to near the tropopause. GOCART

ACPD
13, 19751–19835, 2013

simulation shows sulfate aerosol from that eruption spreading to the Arctic and subarctic as well as the northern part of East Asia (Mongolia and Northern China), and lasting for several months. On annual average for the years included in Fig. 9, extra-regional volcanic sources contribute 0.01–0.03 of sulfate AOD to the EAS region. If we only select sulfur from combustion sources, the correlation between SO_2 emission and sulfate AOD is much tighter (R = 0.973).

5.2 Factors controlling dust emission and loading

We examine two phenomena related to dust emission and transport: the plausible reasons for the changes of dust loading in North Africa, the Middle East, and Central Asia, and the continuous decrease of dust in the tropical North Atlantic (Fig. 6a and b). These changes seem to be consistent between multiple satellite observations and the model.

As we have described in Sect. 2, dust emission in the GOCART model is calculated from Eq. (1). Two key parameters that determine the emission amount are 10 m wind speed, $u_{10\,m}$, and the ground wetness w that is imbedded in the threshold velocity u_t – the stronger the $u_{10\,m}$ and the lower the w, the larger the dust emission. Although $u_{10\,m}$ is the driving force for lifting dust from the ground, w acts as a switch for dust emission depending on whether w is below (emission on) or above (emission off) a threshold value (currently 0.35 in GOCART); meanwhile, it also determines the u_t when w is above the threshold (Ginoux et al., 2001). By examining the dust emission and AOD changes calculated by GOCART and the meteorological variables $u_{10\,m}$ and w from MERRA over major dust regions of North Africa (Sahara and Sahel), the Middle East, and Central Asia (Fig. 10), we find that w plays a more important role in regulating dust emission in Central Asia and the Middle East than in the Sahara and Sahel because the surface is generally wetter, especially in Central Asia where dust emission seems to be mostly determined by the w region-wise (E and w are negatively correlated with R = −0.67). Therefore, we attribute the increase of dust AOD in Central Asia between 2000–2001 and 2008–2009 mostly to a dryer surface in the later years, whereas in the Middle East the change of dust emission responds to both $u_{10\,m}$ and w changes, and

ACPD
13, 19751–19835, 2013

in this case, the $u_{10\,m}$ provides a stronger forcing. Figure 10 also shows a decreasing dust emission trend from the mid-1980s to the mid 2000s in both the Sahara (SHR) and Sahel (SHL), with a stronger decrease in the Sahel. This decrease can be attributed mostly to the weakening of the 10 m wind strength, considering the high correlation between the emission and 10 m winds over both regions. The model-calculated reduction of dust emissions and winds in the Sahel is supported by long-term observations (1984–2010) at seven World Meteorological Organization (WMO) weather stations in the Sahel, all showing decreasing 10 m wind speed and dust event frequency (Cowie et al., 2013).

The different AOD plots for selected time segments in Fig. 6 reveal that dust in the tropical North Atlantic decreased between the late 1980s and the late 2000s. This general decrease was reported in several previous studies that linked the decrease to an increase of sea surface temperature (SST) in the North Atlantic (Wong et al., 2008; Foltz and McPhaden, 2008; Wang et al., 2012) or the increased precipitation in the Sahel (Mishchenko and Geogdzhayev, 2007; Wang et al., 2012). Studies have also shown that dust export from North Africa is to some extent controlled by the North Atlantic Oscillation (NAO), a climate phenomenon in the North Atlantic Ocean that represents fluctuations in the sea level pressure difference between the Icelandic low and the Azores high (e.g., Hurrell, 1995; Hurrell et al., 2003); stronger dust outflow is expected with more positive NAO (e.g., Moulin et al., 1997; Ginoux et al., 2004; Chiapello et al., 2005). We examine the GOCART calculated dust quantities from 1980 to 2009 together with the Hurrell annual NAO index, SST, and precipitation from MERRA in Fig. 11. The correlation coefficients between dust AOD in the tropical North Atlantic and various parameters are listed on the last panel. Figure 11 suggests that the dust AOD in the tropical North Atlantic is most positively correlated with the Sahel dust emission ($R = 0.72$) and mostly negatively correlated with the North Atlantic SST ($R = -0.69$); it is also correlated with dust emission in the Sahara ($R = 0.52$) and anti-correlated with precipitation (implying dust removal) over the tropical North Atlantic ($R = -0.58$). Although the dust AOD change seems to be associated with the phase and strength

ACPD
13, 19751–19835, 2013

of NAO, the correlation is not that strong (R = 0.44). Therefore, the decreasing trend of dust AOD in the tropical North Atlantic during the past 30 yr appears connected mostly to the reduction of dust emissions in the Sahel and the increased precipitation over the North Atlantic. These are probably all driven by the SST increase that changes the surface pressure, atmospheric dynamics, and precipitation, affecting the dust emissions in the source region and transport to the North Atlantic. Although studies have pointed out that a warmer North Atlantic would produce wetter conditions and lower dust emission in Sahel, and thus less dust in North Atlantic (Foltz and McPhaden, 2008; Wang et al., 2012), the MERRA reanalysis does not show increased precipitation over the Sahel (dotted line in panel c in Fig. 11) as SST increases; rather, it yields a precipitation trend over the North Atlantic that removes dust more efficiently. Our results show that the dust emission in the Sahel is more controlled by wind speeds than ground wetness; the latter is directly related to precipitation in the region (Fig. 10). However, the MERRA precipitation trends might be influenced by a change over time of the observing system used in generating the reanalysis, rather than the "real" trends, especially over the ocean (Bosilovich et al., 2011). As such, our interpretation of the causal effects of dust trends may have to be reassessed after any inconsistencies induced by the observing system change in MERRA are removed (M. Bosilovich, NASA GSFC, personal communication, 2012).

5.3 Global and regional trends and attributions of combustion aerosols

Table 4 lists the model-calculated AOD and the percentage from combustion sources in the 15 land regions and 12 ocean regions discussed in Sect. 4, plus the Arctic, the Antarctic, and global averages of land, ocean, and total, in 1980, 1990, 2000, and 2009, to symbolize the global and regional changes of aerosols during the 30 yr period. The last two panels in Fig. 4 show the model-calculated and MODIS-derived 550 nm AOD attributed to combustion (FF + BB) aerosols in 2001, revealing geographic differences in the relative abundance of combustion aerosols that are mostly of anthropogenic origin. Among the major Northern Hemisphere pollution regions, Europe shows the

ACPD
13, 19751–19835, 2013

largest reduction in combustion AOD fraction (−27 %) from 1980 to 2009, and South Asia shows the largest increase (+22 %). Over ocean, the largest reduction of combustion AOD fraction (−16 %) is over the northern part of the North Atlantic (NAT), whereas the largest increase takes place over the North Indian Ocean (+15 %), mostly resulting from emission changes over Europe and South Asia, respectively. Over the Arctic, the combustion AOD fraction has been reduced from over 50 % in 1980 and 1990 to just a little over 30 % in 2000 and 2009, more in line with the European and Russian pollution reduction, although recent studies suggest that Asian pollution is increasingly influencing the pollution level in the Arctic (e.g., Fisher et al., 2010; Bian et al., 2013). Over land, the combustion source accounts for 38 % of AOD in 1980 and 33 % in 2009, whereas over ocean the corresponding percentages are 31 % and 27 %, respectively. The global average of about 30 % FF + BB fraction in this study is lower than our previous model simulation, which estimated the fraction at more than 40 % (Chin et al., 2009), largely because a much higher biomass burning emission (about 70 % higher) was assumed in that study. As we have seen in Figs. 6 and 7, our simulations suggest that the biomass burning emission from A2-ACCMIP in this study may be too low.

Remarkably, even with large changes of anthropogenic and natural emissions (Fig. 2a), the global averaged annual AOD values over land, ocean, and land + ocean only vary within ±0.01 in the years of decadal increments, i.e., no trends or variations over land or ocean on the global annual scale, which is in contrast with regional-scale changes in the source regions over land and continental downwind regions over ocean. This is because opposite trends over different regions cancel each other in the global average. Clearly, using global average values is not sufficient or even not useful for assessing aerosol trends; such an assessment has to be performed at regional scales in a global context.

Results in Table 4 and our analysis in previous sections also suggest that there are trends and inter-annual variability of "natural aerosols", such as dust and volcanoes. Anthropogenic aerosol forcing is considered as a perturbation of the natural state or "background". However, the background is not constant; it exhibits large spatial and

ACPD
13, 19751–19835, 2013

temporal variations, creating challenges for anthropogenic forcing estimation, especially with "measurement-based" approaches that require detecting perturbation signals as deviations from the natural background.

6 Conclusions

We have presented an assessment of atmospheric aerosol sources and regional trends during the last three decades (1980–2009), based on a GOCART model analysis of multi-decadal, multi-platform data. Our analysis is performed over 15 land regions and 12 ocean regions, with land region domains determined mostly by geopolitical boundaries. Such regional definitions are appropriate not only for assessing the environmental effects of emission changes that are often tied to policy or economic development within the geopolitical regions, but also for more accurately addressing the transboundary transport. The model-derived multi-decadal AOD variations within each region have been compared with seven satellite products and ground-based AERONET sun photometer network observations. In-situ measurements of aerosol and precursor concentrations from several surface networks acquitted during different periods within the 30 yr time frame have also been compared with the model results. During the past three decades, large volcanic eruptions of El Chichón in 1982 and Pinatubo in 1991 exerted profound and lasting effects on AOD everywhere on the globe, although they have had little impact on surface aerosol concentrations. Our analysis concentrates on the years having minimal Piniatubo and El Chichón influences.

Over land regions dominated by pollution aerosols, the 30 yr AOD and surface concentration trends are generally consistent with the direction of the regional pollutant emission changes. All observations and model show that the largest reduction of AOD and surface concentration have occurred over Europe, with the late 2000s AOD values nearly half and surface sulfate concentration less than half of their values in the early 1980s. Regions of North America (Canada, USA, and Central America) and Russia have also exhibited various degrees of AOD reductions. On the other hand, East Asia

ACPD
13, 19751–19835, 2013

and South Asia show AOD increases. Even though these changes are in line with the combustion emission trends within the region, relatively large contributions of natural aerosols (dust, volcanic) in Asia make the total AOD changes less directly connected to pollutant emissions trends compared with Europe. Over the Arctic, the model and long-term measurements show a significant decrease in surface sulfate concentrations since the early 1990s, aligned with the decreasing trends over Europe, as the transport of European pollution was the main source of Arctic surface sulfate. There has been virtually no long-term satellite data over the polar regions, but the model also suggests a decreasing AOD trend in the Arctic from 1980 to 2009 at a slower rate than the decrease of surface sulfate, because the column AOD is more affected by the long-range transport from mid-latitudes, especially in recent decades from increased Asian anthropogenic emissions. Although long-range transport affects aerosol loading in regions downwind, the model shows that within polluted regions of the USA, Europe, East Asia, and South Asia the surface concentrations of sulfate, BC, and OM aerosols are highly correlated with regional emissions, with correlation coefficients above 0.9. The correlation between regional emissions and AOD for a given species is less well correlated because of extra-regional aerosol contributions from long-range transport, especially for carbonaceous aerosols (BC and OM) over the US, presumably due to transpacific transport from Asia, and sulfate over East Asia, seemingly from volcanic sources within and outside the region that usually remain aloft longer than boundary layer pollution aerosols.

Over major dust source regions, model analysis of dust emission and its controlling parameters indicates that the change of dust emissions over the Sahara and Sahel responds mostly to near-surface wind speed changes, but over Central Asia, ground wetness is the primary influence. In the Middle East, both wind and ground wetness play important roles in regulating dust emissions. Although there are significant seasonal and inter-annual variabilities of dust distributions, both satellite observations and model simulations show a general decreasing trend of dust in the tropical Atlantic during the last three decades, which seems to be most closely related to a reduction of

ACPD
13, 19751–19835, 2013

dust emission in the Sahel and an increase of precipitation over the North Atlantic, both likely the result of a North Atlantic Ocean warming trend (SST increase) that drives atmospheric circulation and precipitation changes.

Over most ocean areas other than the tropical North Atlantic, aerosol changes are generally much weaker than over land, although close to the continents, they are usually in the same direction as the neighboring land. The AOD tendencies among different satellite data over ocean can be inconsistent, primarily due to AOD values so low that they fall within the range of retrieval uncertainty.

Globally, the model estimates that aerosols from fossil fuel/biofuel combustion and biomass burning, collectively combustion aerosols that are mostly of anthropogenic origin, contribute about 1/3 to the mid-visible AOD, with a higher fraction over land than ocean, and higher in the 1980s than the 2000s. This fraction is likely to represent a lower limit, as the model generally underestimates biomass burning aerosols, excludes some anthropogenic aerosols such as nitrate and the secondary organic aerosol from anthropogenic sources, and overestimates dust aerosols.

Despite the significant changes in aerosol sources, concentrations, and AOD over many regions, model-calculated global averaged AOD values show basically no trends over land or ocean on a global, annual scale, because increases and decreases in different regions tend to cancel each other in the global average. This highlights the need for regional-scale analyses, as global average values conceal significant regional changes that have occurred over the years, and are thus not sufficient for assessing aerosol trends.

Acknowledgements. We thank the IMPROVE, EMEP, and AERONET networks for making their data available on line. Site PIs and data managers of these networks are gratefully acknowledged. We also thank the Goddard Earth Science Data and Information Services Center for providing gridded satellite products of SeaWiFS, MISR, and MODIS through their Giovanni website. This work is supported by NASA's Modeling, Analysis, and Prediction (MAP) program and the Atmospheric Composition, Modeling, and Analysis Program (ACMAP).

ACPD
13, 19751–19835, 2013

References

Andreae, M. O. and Merlet, P.: Emission of trace gases and aerosols from biomass burning, Global Biogeochem. Cy., 15, 955–966, 2001.

Andres, R. J. and Kasgnoc, A. D.: A time-averaged inventory of subaerial volcanic sulfur emissions, J. Geophys. Res., 103, 25251–25261, 1998.

Berresheim, H. and Jaeschke, W.: The Contribution of volcanoes to the global atmospheric sulfur budget, J. Geophys. Res., 88, 3732–3740, 1983.

Bian, H., Colarco, P. R., Chin, M., Chen, G., Rodriguez, J. M., Liang, Q., Blake, D., Chu, D. A., da Silva, A., Darmenov, A. S., Diskin, G., Fuelberg, H. E., Huey, G., Kondo, Y., Nielsen, J. E., Pan, X., and Wisthaler, A.: Source attributions of pollution to the Western Arctic during the NASA ARCTAS field campaign, Atmos. Chem. Phys., 13, 4707–4721, doi:10.5194/acp-13-4707-2013, 2013.

Bluth, G. J. S., Doiron, S. D., Schnetzler, C. C., Krueger, A. J., and Walter, L. S.: Global tracking of the sulfur dioxide clouds from the June 1991 Mount Pinatubo eruptions, Geophys. Res. Lett., 19, 151–154, 1992.

Bosilovich, M. G., Robertson, F. R., and Chen, J.: Global energy and water budgets in MERRA, J. Climate, 24, 5721–5739, 2011.

Brown, M. E., Pinzon, J. E., Didan, K., Morisette, J. T., and Tucker, C. J.: Evaluation of the consistency of long-term NDVI time series derived from AVHRR, SPOT-Vegetation, SeaWIFS, MODIS and LandSAT ETM+, IEEE T. Geosci. Remote, 44, 1787–1793, 2006.

Chan, P. K., Zhao, X., and Heidinger, A. K.: Long-term aerosol climate data record derived from operational AVHRR satellite observations, Dataset Papers in Geosciences, 2013, 140791, doi:10.7167/2013/140791, 2013.

Chiacchio, M., Ewen, T., Wild, M., Chin, M., and Diehl, T.: Decadal variability of aerosol optical depth in Europe and its relationship to the temporal shift of the North Atlantic Oscillation in the realm of dimming and brightening, J. Geophys. Res., 116, D02108, doi:10.1029/2010JD014471, 2011.

Chiapello, I., Moulin, C., and Prospero, J. M.: Understanding the long-term variability of African dust transport across the Atlantic as recorded in both Barbados surface concentrations and large-scale Total Ozone Mapping Spectrometer (TOMS) optical thickness, J. Geophys. Res., 110, D18S10, doi:10.1029/2004JD005132, 2005.

ACPD
13, 19751–19835, 2013

Chin, M., Jacob, D. J., Gardner, G. M., Foreman-Fowler, M. S., Spiro, P. A., and Savoie, D. L.: A global three-dimensional model of tropospheric sulfate, J. Geophys. Res., 101, 18667–18690, 1996.

Chin, M., Rood, R. B., Lin, S.-J., Müller, J.-F., and Thompson, A. M.: Atmospheric sulfur cycle in the global mdel GOCART: model description and global properties, J. Geophys. Res., 105, 24661–24687, 2000.

Chin, M., Ginoux, P., Kinne, S., Torres, O., Holben, B. N., Duncan, B. N., Martin, R. V., Logan, J. A., Higurashi, A., and Nakajima, T.: Tropospheric aerosol optical thickness from the GOCART model and comparisons with satellite and sunphotometer measurements, J. Atmos. Sci., 59, 461–483, 2002.

Chin, M., Chu, D. A., Levy, R., Remer, L., Kaufman, Y., Holben, B. N., Eck, T., Ginoux, P., and Gao, Q.: Aerosol composition and distributions in the Northern Hemisphere during ACE-Asia: Results from global model, satellite observations, and surface sunphotometer measurements, J. Geophys. Res., 109, D23S90, doi:10.1029/2004JD004829, 2004.

Chin, M., Diehl, T., Ginoux, P., and Malm, W.: Intercontinental transport of pollution and dust aerosols: implications for regional air quality, Atmos. Chem. Phys., 7, 5501–5517, doi:10.5194/acp-7-5501-2007, 2007.

Chin, M., Diehl, T., Dubovik, O., Eck, T. F., Holben, B. N., Sinyuk, A., and Streets, D. G.: Light absorption by pollution, dust, and biomass burning aerosols: a global model study and evaluation with AERONET measurements, Ann. Geophys., 27, 3439–3464, doi:10.5194/angeo-27-3439-2009, 2009.

Collaud Coen, M., Andrews, E., Asmi, A., Baltensperger, U., Bukowiecki, N., Day, D., Fiebig, M., Fjaeraa, A. M., Flentje, H., Hyvärinen, A., Jefferson, A., Jennings, S. G., Kouvarakis, G., Lihavainen, H., Lund Myhre, C., Malm, W. C., Mihapopoulos, N., Molenar, J. V., O'Dowd, C., Ogren, J. A., Schichtel, B. A., Sheridan, P., Virkkula, A., Weingartner, E., Weller, R., and Laj, P.: Aerosol decadal trends – Part 1: In-situ optical measurements at GAW and IMPROVE stations, Atmos. Chem. Phys., 13, 869–894, doi:10.5194/acp-13-869-2013, 2013.

Cowie, S., Knippertz, P., and Marsham, J.: Are vegetation-related roughness changes the cause of the recent decrease in dust emission from Sahel?, Geophys. Res. Lett., 40, 1866–1872, doi:10.1002/grl.50273, 2013.

Dey, S. and Di Girolamo, A.: A decade of change in aerosol properties over the Indian subcontinent, Geophys. Res. Lett., 38, L14811, doi:10.1029/2011GL048153, 2011.

ACPD
13, 19751–19835, 2013

Diehl, T., Heil, A., Chin, M., Pan, X., Streets, D., Schultz, M., and Kinne, S.: Anthropogenic, biomass burning, and volcanic emissions of black carbon, organic carbon, and SO_2 from 1980 to 2010 for hindcast model experiments, Atmos. Chem. Phys. Discuss., 12, 24895–24954, doi:10.5194/acpd-12-24895-2012, 2012.

Drury, E., Jacob, D. J., Wang, J., Spurr, R. J. D., and Chance, K.: Improved algorithm for MODIS satellite retrievals of aerosol optical depths over Western North America, J. Geophys. Res., 113, D16204, doi:10.1029/2007JD009573, 2008.

Dubovik, O., Sinyuk, A., Lapyonok, T., Holben, B. N., Mishchenko, M., Yang, P., Eck, T. F., Volten, H., Muñoz, O., Veihelmann, B., van der Zande, W. J., Leon, J.-F., Sorokin, M., and Slutsker, I.: Application of spheroid models to account for aerosol particle nonsphericity in remote sensing of desert dust, J. Geophys. Res., 111, D11208, doi:10.1029/2005JD006619, 2006.

Eck, T. F., Holben, B. N., Reid, J. S., Dubovik, O., Smirnov, A., O'Neill, N. T., Slutsker, I., and Kinne, S.: Wavelength dependence of the optical depth of biomass burning, urban, and desert dust aerosols, J. Geophys. Res., 104, 31333–31349, 1999.

Edwards, D. P., Emmons, L. K., Hauglustaine, D. A., Chu, D. A., Gille, J. C., Kaufman, Y. J., Pétron, G., Yurganov, L. N., Giglio, L., Deeter, M. N., Yudin, V., Ziskin, D. C., Warner, J., Lamarque, J.-F., Francis, G. L., Ho, S. P., Mao, D., Chen, J., Grechko, E. I., and Drummond, J. R.: Observations of carbon monoxide and aerosols from the Terra satellite: Northern Hemisphere variability, J. Geophys. Res., 109, D24202, doi:10.1029/2004JD004727, 2004.

Fisher, J. A., Jacob, D. J., Purdy, M. T., Kopacz, M., Le Sager, P., Carouge, C., Holmes, C. D., Yantosca, R. M., Batchelor, R. L., Strong, K., Diskin, G. S., Fuelberg, H. E., Holloway, J. S., Hyer, E. J., McMillan, W. W., Warner, J., Streets, D. G., Zhang, Q., Wang, Y., and Wu, S.: Source attribution and interannual variability of Arctic pollution in spring constrained by aircraft (ARCTAS, ARCPAC) and satellite (AIRS) observations of carbon monoxide, Atmos. Chem. Phys., 10, 977–996, doi:10.5194/acp-10-977-2010, 2010.

Foltz, G. R. and McPhaden, M. J.: Trends in Saharan dust and tropical Atlantic climate during 1980–2006, Geophys. Res. Lett., 35, L20706, doi:10.1029/2008GL035042, 2008.

Gantt, B., Meskhidze, N., Facchini, M. C., Rinaldi, M., Ceburnis, D., and O'Dowd, C. D.: Wind speed dependent size-resolved parameterization for the organic mass fraction of sea spray aerosol, Atmos. Chem. Phys., 11, 8777–8790, doi:10.5194/acp-11-8777-2011, 2011.

ACPD
13, 19751–19835, 2013

Generoso, S., Bey, I., Attie, J.-L., and Bréon, F.-M.: A stellite- and model-based assessment of the 2003 Russian fires: impact on the Arctic region, J. Geophys. Res., 112, D15301, doi:10.1029/2006JD008344, 2007.

Ginoux, P., Chin, M., Tegen, I., Prospero, J., Holben, B., Dubovik, O., and Lin, S.-J.: Sources and global distributions of dust aerosols simulated with the GOCART model, J. Geophys. Res. 106, 20255–20273, 2001.

Ginoux, P., Prospero, J., Torres, O., and Chin, M.: Long-term simulation of dust distribution with the GOCART model: correlation with the North Atlantic Oscillation, Environ. Modell. Softw., 19, 113–128, 2004.

Gong, S.: A parameterization of sea-salt aerosol source function for sub- and super-micron particles, Global Biogeochem. Cy., 17, 1097, doi:10.1029/2003GB002079, 2003.

Granier, C., Bessagnet, B., Bond, T., D'Angiola, A., Gon, H. D. v. d., Frost, G. J., Heil, A., Kaiser, J. W., Kinne, S., Klimont, Z., Kloster, S., Lamarque, J.-F., Liousse, C., Masui, T., Meleux, F., Mieville, A., Ohara, T., Raut, J.-C., Riahi, K., Schultz, M. G., Smith, S. J., Thompson, A., van Aardenne, J., van der Werf , G. R., and van Vuuren, D. P.: Evolution of anthropogenic and biomass burning emissions of air pollutants at global and regional scales during the 1980–2010 period, Climatic Change, 109, 163–190, doi:10.1007/s10584-011-0154-1, 2011.

Hadley, O. L., Ramanathan, V., Carmichael, G. R., Tang, Y., Corrigan, C. E., Roberts, G. C., and Mauger, G. S.: Trans-Pacific transport of black carbon and fine aerosols ($D < 2.5\,\mu m$) into North America, J. Geophys. Res., 112, D05309, doi:10.1029/2006JD007632, 2007.

Herman, J. R., Bhartia, P. K., Torres, O., Hsu, C., and Seftor, C.: Global distribution of UV-absorbing aerosols from Nimbus 7/TOMS data, J. Geophys. Res., 102, 16911–16922, 1997.

Hess, M., Koepke, P., and Schult, I.: Optical properties of aerosols and clouds: the software package OPAC, B. Am. Meteorol. Soc., 79, 831–844, 1998.

Holben B. N., Eck, T. F., Slutsker, I., Tanré, D., Buis, J. P., Setzer, A., Vermote, E., Reagan, J. A., Kaufman, Y., Nakajima, T., Lavenu, F., Jankowiak, I., and Smirnov, A.: AERONET – a federated instrument network and data archive for aerosol characterization, Remote Sens. Environ., 66, 1–16, 1998.

Holben, B. N., Tanré, D., Smirnov, A., Eck, T. F., Slutsker, I., Abuhassan, N., Newcomb, W. W., Schafer, J., Chatenet, B., Lavenue, F., Kaufman, Y. J., Vande Castle, J., Setzer, A., Markham, B., Clark, D., Frouin, R.,Halthore, R., Karnieli, A., O'Neill, N.T., Pietras, C., Pinker, R. T., Voss, K., and Zibordi, G.: An emerging ground-based aerosol climatology: aersol optical depth from AERONET, J. Geophys. Res., 106, 12067–12097, 2001.

ACPD
13, 19751–19835, 2013

Hsu, N. C., Herman, J. R., Bhartia, P. K., Seftor, C. J., Torres, O., Thompson, A. M., Gleason, J. F., Eck, T. F., and Holben, B. N.: Detection of biomass burning smoke from TOMS measurements, Geophys. Res. Lett., 23, 745–748, 1996.

Hsu, N. C., Tsay, S.-C., King, M. D., and Herman, J. R.: Aerosol properties over bright-reflecting source regions, IEEE T. Geosci. Remote, 42, 557–569, 2004.

Hsu, N. C., Gautam, R., Sayer, A. M., Bettenhausen, C., Li, C., Jeong, M. J., Tsay, S.-C., and Holben, B. N.: Global and regional trends of aerosol optical depth over land and ocean using SeaWiFS measurements from 1997 to 2010, Atmos. Chem. Phys., 12, 8037–8053, doi:10.5194/acp-12-8037-2012, 2012.

HTAP 2010: Hemispheric Transport of Air Pollution 2010. Part A: Ozone and Particulate Matter, Air Pollution Studies No. 17, edited by: Dentener, F., Keating, T., and Akimoto, H., United Nations, New York, 2010.

Hurrell, J. W.: Decadal trend in the North Atlantic Oscillation: regional temperatures and precipitations, Science, 269, 676–679, 1995.

Hurrell, J. W., Kushnir, Y., Visbeck, M., and Ottersen, G.: An overview of the North Atlantic Oscillation, in: The North Atlantic Oscillation, Climatic Significance and Environmental Impact, edited by: Hurrell, J. W., Kushnir, Y., Ottersen, G., and Visbeck, M., AGU Geophysical Monograph, vol. 134, 1–35, 2003.

Husar, R. B., Prospero, J. M., and Stowe, L. L.: Characterization of tropospheric aerosols over the oceans with the NOAA advanced very high resolution radiometer optical thickness operational product, J. Geophys. Res., 102, 16889–16909, 1997.

Jaeglé, L., Quinn, P. K., Bates, T. S., Alexander, B., and Lin, J.-T.: Global distribution of sea salt aerosols: new constraints from in situ and remote sensing observations, Atmos. Chem. Phys., 11, 3137–3157, doi:10.5194/acp-11-3137-2011, 2011.

Kahn, R. A., Garay, M. J., Nelson, D. L., Yau, K. K., Bull, M. A., Gaitley, B. J.,Martonchik, J. V., and Levy, R. C.: Satellite-derived aerosol optical depth over dark water from MISR and MODIS: comparisons with AERONET and implications for climatological studies, J. Geophys. Res., 112, D18205, doi:10.1029/2006JD008175, 2007.

Kahn, R. A., Nelson, D. L., Garay, M., Levy, R. C., Bull, M. A., Diner, D. J., Martonchik, J. V., Paradise, S. R., and Hansen, E. G., and Remer, L. A.: MISR Aerosol product attributes, and statistical comparisons with MODIS, IEEE T. Geosci. Remote, 47, 4095–4114, 2009.

Kahn, R. A., Gaitley, B. J., Garay, M. J., Diner, D. J., Eck, T., Smirnov, A., and Holben, B. N.: Multiangle Imaging SpectroRadiometer global aerosol product assessment by comparison with

ACPD
13, 19751–19835, 2013

the Aerosol Robotic Network, J. Geophys. Res., 115, D23209, doi:10.1029/2010JD014601, 2010.
Kalashnikova, O. V., Garay, M. J., Martonchik, J. V., and Diner, D. J.: MISR Dark Water aerosol retrievals: operational algorithm sensitivity to particle non-sphericity, Atmos. Meas. Tech. Discuss., 6, 1589–1648, doi:10.5194/amtd-6-1589-2013, 2013.
Karnieli, A., Derimian, Y., Indoitu, R., Panov, N., Levy, R. C., Remer, L. A., Maenhaut, W., and Holben, B. N.: Temporal trend in anthropogenic sulfur aerosol transport from Central and Eastern Europe to Israel, J. Geophys. Res., 114, D00D19, doi:10.1029/2009JD011870, 2009.
Kaufman, Y. J., Tanré, D., Remer, L., Vermote, E., Chu, A., and Holben, B. N.: Operational remote sensing of tropo- spheric aerosol over land from EOS moderate resolution imaging spectroradiometer, J. Geophys. Res., 102, 17051– 17067, 1997.
Kaufman, Y. J., Boucher, O., Tanré, D., Chin, M., Remer, L. A., and Takemura, T.: Aerosol anthropogenic component estimated from satellite data, Geophys. Res. Lett., 32, L17804, doi:10.1029/2005GL023125, 2005.
Kim, D., Chin, M., Bian, H., Tan, Q., Brown, M. E., Zheng, T., You, R., Diehl, T., Ginoux, P., and Kucsera, T.: The effect of the dynamic surface bareness on dust source function, emission, and distribution, J. Geophys. Res., 118, 1–16, doi:10.1029/2012JD017907, 2013.
Koch, D., Jacob, D., Tegen, I., Rind, D., and Chin, M.: Tropospheric sulfur simulations and sulfate direct radiative forcing in the GISS GCM, J. Geophys. Res., 104, 23799–23823, 1999.
Koffi, B., Schulz, M., Bréon, F.-M., Griesfeller,J., Winker, D., Balkanski, Y., Bauer, S., Berntsen,T., Chin, M., Collins, W. D., Dentener, F., Diehl, T., Easter, R., Ghan, S., Ginoux, P., Gong, S., Horowitz, L. W., Iversen, T., Kirkevåg, A., Koch, D., Krol, M., Myhre, G., Stier, P., and Takemura, T.: Application of the CALIOP layer product to evaluate the vertical distribution of aerosols estimated by global models: AeroCom phase I results, J. Geophys. Res., 117, D10201, doi:10.1029/2011JD016858, 2012.
Lamarque, J.-F., Bond, T. C., Eyring, V., Granier, C., Heil, A., Klimont, Z., Lee, D., Liousse, C., Mieville, A., Owen, B., Schultz, M. G., Shindell, D., Smith, S. J., Stehfest, E., Van Aardenne, J., Cooper, O. R., Kainuma, M., Mahowald, N., McConnell, J. R., Naik, V., Riahi, K., and van Vuuren, D. P.: Historical (1850–2000) gridded anthropogenic and biomass burning emissions of reactive gases and aerosols: methodology and application, Atmos. Chem. Phys., 10, 7017–7039, doi:10.5194/acp-10-7017-2010, 2010.

ACPD
13, 19751–19835, 2013

Lamarque, J.-F., Shindell, D. T., Josse, B., Young, P. J., Cionni, I., Eyring, V., Bergmann, D., Cameron-Smith, P., Collins, W. J., Doherty, R., Dalsoren, S., Faluvegi, G., Folberth, G., Ghan, S. J., Horowitz, L. W., Lee, Y. H., MacKenzie, I. A., Nagashima, T., Naik, V., Plummer, D., Righi, M., Rumbold, S. T., Schulz, M., Skeie, R. B., Stevenson, D. S., Strode, S., Sudo, K., Szopa, S., Voulgarakis, A., and Zeng, G.: The Atmospheric Chemistry and Climate Model Intercomparison Project (ACCMIP): overview and description of models, simulations and climate diagnostics, Geosci. Model Dev., 6, 179–206, doi:10.5194/gmd-6-179-2013, 2013.

Lana, A., Bell, T. G., Simó, R., Vallina, S. M., Ballabrera-Poy, J., Kettle, A. J., Dachs, J., Bopp, L., Saltzman, E. S., Stefels, J., Johnson, J. E., and Liss, P. S.: An updated climatology of surface dimethlysulfide concentrations and emission fluxes in the global ocean, Global Biogeochem. Cy., 25, GB1004, doi:10.1029/2010GB003850, 2011.

Leibensperger, E. M., Mickley, L. J., Jacob, D. J., Chen, W.-T., Seinfeld, J. H., Nenes, A., Adams, P. J., Streets, D. G., Kumar, N., and Rind, D.: Climatic effects of 1950–2050 changes in US anthropogenic aerosols – Part 1: Aerosol trends and radiative forcing, Atmos. Chem. Phys., 12, 3333–3348, doi:10.5194/acp-12-3333-2012, 2012.

Levy, R. C., Remer, L. A., Kleidman, R. G., Mattoo, S., Ichoku, C., Kahn, R., and Eck, T. F.: Global evaluation of the Collection 5 MODIS dark-target aerosol products over land, Atmos. Chem. Phys., 10, 10399–10420, doi:10.5194/acp-10-10399-2010, 2010.

Levy, R. C., Mattoo, S., Munchak, L. A., Remer, L. A., Sayer, A. M., and Hsu, N. C.: The Collection 6 MODIS aerosol products over land and ocean, Atmos. Meas. Tech. Discuss., 6, 159–259, doi:10.5194/amtd-6-159-2013, 2013.

Li, Z., Zhao, X., Kahn, R., Mishchenko, M., Remer, L., Lee, K.-H., Wang, M., Laszlo, I., Nakajima, T., and Maring, H.: Uncertainties in satellite remote sensing of aerosols and impact on monitoring its long-term trend: a review and perspective, Ann. Geophys., 27, 2755–2770, doi:10.5194/angeo-27-2755-2009, 2009.

Luo, Y., Lu, D., Zhou, X., Li, W., and He, Q.: Characteristics of the spatial distribution and yearly variation of aerosol optical depth over China in last 30 years, J. Geophys. Res., 106, 14501–14513, 2001.

Malm, W. C., Sisler, J. F., Huffman, D., Eldred, R. A., and Cahill, T. A.: Spatial and seasonal trends in particle concentration and op- tical extinction in the United States, J. Geophys. Res., 99, 1347–1370, 1994.

ACPD
13, 19751–19835, 2013

Malm, W. C., Day, D. E., Kreidenweis, S. M., Collett, J. L., and Lee, T.: Humidity-dependent optical properties of fine particles during the Big Bend Regional Aerosol Visibility Observational Study, J. Geophys. Res., 108, 4279, doi:10.1029/2002JD002998, 2003.
Maring, H., Savoie, D., Izaguirre, M., McCormick, C., Arimoto, R., Prospero, J., and Pilinis, C.: Aerosol physical and optical properties and their relationship to aerosol composition in the free troposphere at Izaña, Tenerife, Canary Islands during July 1995, J. Geophys. Res., 105, 14677–14700, 2000.
Massie, S. T., Torres, O., and Smith, S. J.: Total Ozone Mapping Spectrometer (TOMS) observations of increases in Asian aerosol in winter from 1979 to 2000, J. Geophys. Res., 109, D18211, doi:10.1029/2004JD004620, 2004.
McCormick, M., Thomason, L. W., and Trepte, C. R.: Atmospheric effects of the Mt Pinatubo eruption, Nature, 373, 399–404, 1995.
McClain, C. R., Cleave, M. L., Feldman, G. C., Gregg, W. W., Hooker, S. B., and Kuring, N.: Science quality SeaWiFS data for global biospheric research, Sea Technol., 39, 10–16, 1998.
Mishchenko, M. I. and Geogdzhayev, I. V.: Satellite remote sensing reveals regional tropospheric aerosol trends, Opt. Express, 15, 7423–7438, 2007.
Mishchenko, M. I., Travis, L. D., Kahn, R. A., and West, R. A.: Modeling phase functions for dustlike tropospheric aerosols using a shape mixture of randomly oriented polydisperse spheroids, J. Geophys. Res., 102, 16831–16847, doi:10.1029/96JD02110, 1997.
Mishchenko, M. I., Geogdzhayev, I. V., Cairns, B., Rossow, W. B., and Lacis, A. A.: Aerosol retrievals over the ocean by use of channels 1 and 2 AVHRR data: sensitivity analysis and preliminary results, Appl. Optics, 38, 7325–41, 1999.
Mishchenko, M. I., Geogdzhayev, I. V., Rossow, W. B., Cairns, B., Carlson, B. E., Lacis, A. A., Liu, L., and Travis, L. D.: Long-term satellite record reveals likely recent aerosol trend, Science, 315, 1543, doi:10.1126/science.1136709, 2007.
Mishchenko, M. I., Liu, L., Geogdzhayev, I. V., Li, J., Carlson, B. E., Lacis, A. A., Cairns, B., and Travis, L. D.: Aerosol retrievals from channel-1 and -2 AVHRR radiances: long-term trends updated and revisited, J. Quant. Spectrosc. Ra., 113, 1974–1980, 2012.
Moorthy, K. K., Babu, S. S., Manoj, M. R., and Satheesh, S. K.: Buildup of aerosols over the Indian Region, Geophys. Res. Lett, 40, 1011–1014, doi:10.1002/grl.50165, 2012.
Moulin, C., Lambert, C. E., Dulac, F., and Dayan, U.: Control of atmospheric export of dust from North Africa by the North Atlantic Oscillation, Nature, 387, 691–694, 1997.

ACPD
13, 19751–19835, 2013

Murphy, D. M., Chow, J. C., Leibensperger, E. M., Malm, W. C., Pitchford, M., Schichtel, B. A., Watson, J. G., and White, W. H.: Decreases in elemental carbon and fine particle mass in the United States, Atmos. Chem. Phys., 11, 4679–4686, doi:10.5194/acp-11-4679-2011, 2011.
Nakajima, T. and Higurashi, A.: A use of two-channel radiances for an aerosol characterization from space, Geophys. Res. Lett., 25, 3815–3818, 1998.
Oman, L. D., Ziemke, J. R., Douglass, A. R., Waugh, D. W., Lang, C., Rodriguez, J. M., and Nielsen, J. E.: The response of tropical tropospheric ozone to ENSO, Geophys. Res. Lett., 38, L13706, doi:10.1029/2011GL047865, 2011.
Petrenko, M., Kahn, R., Chin, M., Soja, A., Kucsera, T., and Harshvardhan: The use of satellite-measured aerosol optical depth to constrain biomass burning emissions source strength in a global model GOCART, J. Geophys. Res., 117, D18212, doi:10.1029/2012JD017870, 2012.
Prospero, J. M.: Long-range transport of mineral dust in the global atmosphere: impact of African dust on the environment of the Southeastern United States, P. Natl. Acad. Sci. USA, 96, 3396–3403, 1999.
Prospero, J. M. and Lamb, P. J.: African droughts and dust transport to the Caribbean: climate change implications, Science, 302, 1024–1027, 2003.
Prospero, J. M., Savoie, D. L., Saltzman, E. S., and Larsen, R.: Impact of oceanic sources of biogenic sulphur on sulphate aerosol concentrations at Mawson, Antarctica, Nature, 350, 221–223, 1991.
Prospero, J. M., Savoie, D. L., and Arimoto, R.: Long-term record of nss-sulfate and nitrate in aerosols on Midway Island, 1981–2000: evidence of increased (now decreasing?) anthropogenic emissions from Asia, J. Geophys. Res., 108, 4019, doi:10.1029/2001JD001524, 2003.
Quinn, P. K., Shaw, G., Andrews, E., Dutton, E. G., Ruoho-Airola, T., and Gong, S. L.: Arctic haze: current trends and knowledge gaps, Tellus B, 59, 99–114, 2007.
Quinn, P. K., Bates, T. S., Baum, E., Doubleday, N., Fiore, A. M., Flanner, M., Fridlind, A., Garrett, T. J., Koch, D., Menon, S., Shindell, D., Stohl, A., and Warren, S. G.: Short-lived pollutants in the Arctic: their climate impact and possible mitigation strategies, Atmos. Chem. Phys., 8, 1723–1735, doi:10.5194/acp-8-1723-2008, 2008.
Rahn, K. A.: Relative importance of North America and Eurasia as sources of Arctic aerosol, Atmos. Environ., 15, 1447–1455, 1981.

ACPD
13, 19751–19835, 2013

Ramachandran, S., Kedia, S., and Srivastava, R.: Aerosol optical depth trends over different regions of India, Atmos. Environ., 49, 338–347, 2012.

Remer, L. A., Kaufman, Y. J., Tanré, D., Mattoo, S., Chu, D. A., Martins, J. V., Li, R.-R., Ichoku, C., Levy, R. C., Kleidman, R. G., Eck, T. F., Vermote, E., and Holben, B. N.: The MODIS aerosol algorithm, products, and validation, J. Atmos. Sci., 62, 947–973, 2005.

Remer, L. A., Kleidman, R. G., Levy, R. C., Kaufman, Y. J., Tanre, D., Mattoo, S., Martins, J. V., Ichoku, C., Koren, I., Yu, H., and Holben, B. N.: Global aerosol climatology from the MODIS satellite sensors, J. Geophys. Res.-Atmos., 113, D14S07, doi:10.1029/2007JD009661, 2008.

Riahi, K., Rao, S., Krey, V., Cho, C., Chirkov, V., Fischer, G., Kindermann, G., Nakicenovic, N., and Rafaj, P.: RCP 8.5 – a scenario of comparatively high greenhouse gas emissions, Climatic Change, 109, 33–57, doi:10.1007/s10584-011-0149-y, 2011.

Rienecker, M. M., Suarez, M. J., Gelaro, R., Todling, R., Bacmeister, J., Liu, E., Bosilovich, M. G., Schubert, S. D., Takacs, L., Kim, G.-K., Bloom, S., Chen, J., Collins, D., Conaty, A., da Silva, A., Gu, W., Joiner, J., Koster, R. D., Lucchesi, R., Molod, A., Owens, T., Pawson, S., Pegion, P., Redder, C. R., Reichle, R., Robertson, F. R., Ruddick, A. G., Sienkiewicz, M., and Woollen, J.: MERRA – NASA's modern-era retrospective analysis for research and applications, J. Climate, 24, 3624–3648, 2011.

Savoie, D. L., Prospero, J. M., Larsen, R. J., and Saltzman, E. S.: Nitrogen and sulfur species in aerosols at Mawson, Antarctica, and their relationship to natural radionuclides, J. Atmos. Chem., 14, 181–204, 1992.

Savoie, D. L., Arimoto, R., Keene, W. C., Prospero, J. M., Duce, R. A., and Galloway, J. N.: Marine biogenic and anthropogenic contributions to nonseasalt sulfate in the marine boundary layer over the North Atlantic Ocean, J. Geophys. Res., 107, 4356, doi:10.1029/2001JD000970, 2002.

Sayer, A. M., Hsu, N. C., Bettenhausen, C., Ahmad, Z., Holben, B. N., Smirnov, A., Thomas, G. E., and Zhang, J.: SeaWiFS Ocean Aerosol Retrieval (SOAR): algorithm, validation, and comparison with other data sets, J. Geophys. Res., 117, D03206, doi:10.1029/2011JD016599, 2012.

Schnetzler, C. C., Bluth, G. J. S., Krueger, A. J., and Walter, L. S.: A proposed volcanic sulfur dioide index (VSI), J. Geophys. Res., 102, 20087–20091, 1997.

ACPD
13, 19751–19835, 2013

Schultz, M. G., Heil, A., Hoelzemann, J. J., Spessa, A., Thonicke, K., Goldammer, J., Held, A. C., Pereira, J. M., and van het Bolscher, M.: Global wildland fire emissions from 1960 to 2000, Global Biogeochem. Cy., 22, GB2002, doi:10.1029/2007GB003031, 2008.

Shaw, G. E. and Stamnes: K.: Arctic haze: perturbation of the Polar radiation budget, Am. NY Acad. Sci., 338, 533–539, 1980.

Shinozuka, Y., Clarke, A. D., Howell, S. G., Kapustin, V. N., and Huebert, B. J.: Sea-salt vertical profiles over the Southern and tropical Pacific oceans: microphysics, optical properties, spatial variability, and variations with wind speed, J. Geophys. Res., 109, D24201, doi:10.1029/2004JD004975, 2004.

Sillmann, J., Pozzoli, L., Vignati, E., Kloster, S., and Feichter, J.: Aerosol effect on climate extremes in Europe under different future scenarios, Geophys. Res. Lett., 40, 1–6, doi:10.1002/grl.50459, 2013.

Smirnov, A., Holben, B. N., Giles, D. M., Slutsker, I., O'Neill, N. T., Eck, T. F., Macke, A., Croot, P., Courcoux, Y., Sakerin, S. M., Smyth, T. J., Zielinski, T., Zibordi, G., Goes, J. I., Harvey, M. J., Quinn, P. K., Nelson, N. B., Radionov, V. F., Duarte, C. M., Losno, R., Sciare, J., Voss, K. J., Kinne, S., Nalli, N. R., Joseph, E., Krishna Moorthy, K., Covert, D. S., Gulev, S. K., Milinevsky, G., Larouche, P., Belanger, S., Horne, E., Chin, M., Remer, L. A., Kahn, R. A., Reid, J. S., Schulz, M., Heald, C. L., Zhang, J., Lapina, K., Kleidman, R. G., Griesfeller, J., Gaitley, B. J., Tan, Q., and Diehl, T. L.: Maritime aerosol network as a component of AERONET – first results and comparison with global aerosol models and satellite retrievals, Atmos. Meas. Tech., 4, 583–597, doi:10.5194/amt-4-583-2011, 2011.

Stoiber, R. E., Williams, S. N., and Huebert, B.: Annual contribution of sulfur dioxide to the atmosphere by volcanoes, J. Volcanol. Geotherm. Res., 33, 1–8, 1987.

Stowe, L. L., Ignatov, A. M., and Singh, R. R.: Development, validation and potential enhancements to the second generation operational aerosol product at NOAA/NESDIS, J. Geophys. Res., 102, 16923–16934, 1997.

Streets, D. G., Wu, Y., and Chin, M.: Two-decadal aerosol trends as a likely explanation of the global dimming/brightening transition, Geophys. Res. Lett., 33, L15806, doi:10.1029/2006GL026471, 2006.

Tanré, D., Kaufman, Y. J., Herman, M., and Mattoo, S.: Remote sensing of aerosol properties over oceans using the MODIS/EOS spectral radiances, J. Geophys. Res., 102, 16971–16988, doi:10.1029/96JD03437, 1997.

ACPD
13, 19751–19835, 2013

Taylor, K. E.: Summarizing multiple aspects of model performance in a single diagram, J. Geophys. Res., 106, 7183–7192, 2001.
Thomas, G. E., Poulsen, C. A., Siddans, R., Sayer, A. M., Carboni, E., Marsh, S. H., Dean, S. M., Grainger, R. G., and Lawrence, B. N.: Validation of the GRAPE single view aerosol retrieval for ATSR-2 and insights into the long term global AOD trend over the ocean, Atmos. Chem. Phys., 10, 4849–4866, doi:10.5194/acp-10-4849-2010, 2010.
Torres, O., Herman, J. R., Ahmad, Z., and Gleason, J.: Derivation of aerosol properties from satellite measurements of back- scattered ultraviolet radiation: theoretical basis, J. Geophys. Res., 103, 17099–17110, 1998.
Torres, O., Bhartia, P. K., Herman, J. R., Sinyuk, A., Ginoux, P., and Holben, B.: A long-term record of aerosol optical depth from TOMS observations and comparison to AERONET measurements, J. Atmos. Sci., 59, 398–413, 2002.
Torres, O., Bhartia, P. K., Sinyuk, A., Welton, E. J., and Holben, B.: Total Ozone Mapping Spectrometer measurements of aerosol absorption from space: comparison to SAFARI 2000 ground-based observations, J. Geophys. Res., 110, D10S18, doi:10.1029/2004JD004611, 2005.
Toth, T. D., Zhang, J., Campbell, J. R., Reid, J. S., Shi, Y., Johnson, R. S., Smirnov, A., Vaughan, M. A., and Winker, D. M.: Investigating enhanced Aqua MODIS aerosol optical depth retrievals over the mid-to-high latitude Southern Oceans through intercomparison with co-located CALIOP, MAN, and AERONET data sets, J. Geophys. Res., 118, 1–15, doi:10.1002/jgrd.50311, 2013.
Tucker, C., Pinzon, J. J. E., Brown, M. E., Slayback, D., Pak, E. W., Mahoney, R., Vermote, E., and El Saleous, N.: An extended AVHRR 8-km NDVI data set compatible with MODIS and SPOT vegetation NDVI data, Int. J. Remote Sens., 26, 4485–4498, 2005.
van der Werf, G. R., Randerson, J. T., Giglio, L., Collatz, G. J., Kasibhatla, P. S., and Arellano Jr., A. F.: Interannual variability in global biomass burning emissions from 1997 to 2004, Atmos. Chem. Phys., 6, 3423–3441, doi:10.5194/acp-6-3423-2006, 2006.
Wang, C., Dong, S., Evan, A. T., Foltz, G. R., and Lee, S.-K.: Multidecadal covariability of North Atlantic sea surface temperature, African dust, Sahel rainfall, and Atlantic hurricanes, J. Climate, 25, 5404–5415, 2012.
Wilson, S. R. and Forgan, B. W.: Aerosol optical depth at Cape Grim, Tasmania, 1986–1999, J. Geophys. Res., 107, 4068, doi:10.1029/2001JD000398, 2002.

ACPD
13, 19751–19835, 2013

Wong, S., Dessler, A. E., Mahowald, N. M., Colarco, P. R., and da Silva, A.: Long-term variability in Saharan dust transport and its link to North Atlantic sea surface temperature, Geophys. Res. Lett., 35, L07812, doi:10.1029/2007GL032297, 2008.

Yu, H., Chin, M., Remer, L. A., Kleidman, R. G., Bellouin, N., Bian, H., and Diehl, T.: Variability of marine aerosol fine-mode fraction and estimates of anthropogenic aerosol component over cloud-free oceans from the Moderate resolution Imaging Spectroradiometer (MODIS), J. Geophys. Res., 114, D10206, doi:10.1029/2008JD010648, 2009.

Yu, H., Chin, M., Winker, D. M., Omar, A. H., Liu, Z., Kittaka, C., and Diehl, T.: Global view of aerosol vertical distributions from CALIPSO lidar measurements and GOCART simulations: regional and seasonal variations, J. Geophys. Res., 115, D00H30, doi:10.1029/2009JD013364, 2010.

Yu, H., Remer, L., Chin, M., Bian, H., Tan, Q., Yuan, T., and Zhang, Y.: Aerosols from overseas rival domestic emissions over North America, Science, 337, 566–569, 2012.

Yu, H., Chin, M., West, J. J., Atherton, C. S., Bellouin, N., Bergmann, D., Bey, I., Bian, H., Diehl, T., Forberth, G., Hess, P., Schulz, M., Shindell, D., Takemura,T., and Tan, Q.: A multimodel assessment of the influence of regional anthropogenic emission reductions on aerosol direct radiative forcing and the role of intercontinental transport, J. Geophys. Res., 118, 700–720, doi:10.1029/2012JD018148, 2013.

Zhang, J. and Reid, J. S.: MODIS Aerosol product analysis for data assimilation: assessment of Level 2 aerosol optical thickness retrievals, J. Geophys. Res., 111, D22207, doi:10.1029/2005JD006898, 2006.

Zhang, J. and Reid, J. S.: A decadal regional and global trend analysis of the aerosol optical depth using a data-assimilation grade over-water MODIS and Level 2 MISR aerosol products, Atmos. Chem. Phys., 10, 10949–10963, doi:10.5194/acp-10-10949-2010, 2010.

Zhao, X.-P., Laszlo, I., Guo, W., Heidinger, A., Cao, C., Jelenak, A., Tarpley, D., and Sullivan, J.: Study of long-term trend in aerosol optical thickness observed from operational AVHRR satellite instrument, J. Geophys. Res., 113, D07201, doi:10.1029/2007JD009061, 2008.

Zhao, X.-P., Chan, P. K., and Heidinger, A. K.: A global survey of the effect of cloud contamination on the aerosol optical thickness and its long-term trend derived from operational AVHRR satellite observations, J. Geophys. Res., 118, 2849–2857, doi:10.1002/jgrd.50278, 2013.

ACPD
13, 19751–19835, 2013

Table 1. Region description, abbreviation, and surface area of 15 land and 12 ocean regions (domains in Fig. 1).

	Region	Abbr.	Area (10^9 m^2)
Land regions:			
1	Canada + Alaska	CAN	13 350
2	United States (Continental)	USA	8200
3	Central America + Mexico	CAM	3900
4	Europe	EUR	7480
5	Russia + Georgia	RUS	18 230
6	Central Asia	CAS	3930
7	East Asia	EAS	12 190
8	South Asia	SAS	5460
9	Southeast Asia	SEA	7640
10	Sahara	SHR	9230
11	Sahel	SHL	2980
12	Middle East	MDE	6650
13	South America	SAM	18 980
14	Rest of Africa	RAF	19 300
15	Australia and New Zealand	ANZ	9260
Ocean regions:			
1	North Atlantic	NAT	20 960
2	Western North Pacific	WNP	10 600
3	Eastern North Pacific	ENP	14 030
4	Central Atlantic	CAT	22 490
5	Western Central Pacific	WCP	23 170
6	Eastern Central Pacific	ECP	29 820
7	North Indian Ocean	NIN	9750
8	Western South Pacific	WSP	17 420
9	Eastern South Pacific	ESP	54 520
10	South Indian Ocean	SIN	42 870
11	South Atlantic	SAT	30 370
12	Southern Ocean	SOU	53 580

ACPD
13, 19751–19835, 2013

Table 2. Observation data used in this study.

Dataset	Location	Period
Satellite AOD:		
AVHRR[a]-CDR	Global, ocean	1981–2009
AVHRR[a]-GACP	Global, ocean	1981–2005
TOMS[b]	Global, land +ocean	1980–1992, 1996–2001
SeaWiFS	Global, land +ocean	1997–2009
MISR	Global, land +ocean	2000–2009
MODIS-Terra	Global, land +ocean	2000–2009
MODIS-Aqua	Global, land +ocean	2002–2009
Sunphotometer AOD:		
AERONET	> 200 sites over the globe	1994–2009
Surface concentration:		
IMPROVE	73 sites in US	1988–2007
EMEP	135 sites in Europe	1980–2008
AMAP	9 sites in or near the Arctic	1980–2009
Univ. Miami	15 sites on islands or coast	1981–2002
Univ. Hawaii	1 site, Mauna Loa, Hawaii	1989–2009

[a] AVHRR instrument aboard 12 different NOAA satellites (NOAA-6, -7, -9, -10, -11, -12, -14, -15, -16, -17, -18, and -19) during the study period.

[b] TOMS instrument aboard the Nimbus-7 satellite between 1979 to 1992 and the Earth Probe satellite between later half of 1996 to 2005. Data quality degraded after 2001 thus not used here. No TOMS data available between 1993 and first half of 1996.

ACPD
13, 19751–19835, 2013

Table 3. Statistics[a] of model comparisons with ground-based observations of monthly averaged quantities.

Network	Quantity	*R*	*E*	*B*	*S*
AERONET (global)	AOD	0.697	0.129	0.919	0.824
IMPROVE (US)	Sulfate	0.834	1.065	1.315	0.877
	BC	0.529	0.243	0.631	0.682
	OC	0.466	1.266	0.564	0.575
	Fine dust	0.586	0.952	1.584	0.772
EMEP (Europe)	SO_2	0.654	4.917	1.892	0.774
	Sulfate	0.534	0.999	1.223	0.752
AMAP (Arctic)	Sulfate	0.743	0.672	1.295	0.870
Univ. Miami (islands)	Sulfate	0.798	0.461	1.043	0.897
	MSA	0.522	0.019	0.539	0.739
	Dust	0.739	21.41	1.974	0.643
	Sea salt	0.410	11.43	1.272	0.664

[a] The statistic quantities include the correlation coefficient *R*, the root-mean-square-error *E*, the mean bias *B* (defined as the ratio of the model results to the data), and the skill score *S* (a combined measure of correlation and standard error between observation and model, see Taylor, 2001).

ACPD
13, 19751–19835, 2013

Table 4. Global and regional annual averaged percentage of 550 nm AOD from combustion (fossil fuel, biofuel, and biomass burning, or FF + BB) sources in 1980, 1990, 2000, and 2009.

Region		AOD and (% from FF + BB)			
		1980	1990	2000	2009
Land regions:					
1	CAN	0.14 (50 %)	0.14 (47 %)	0.13 (35 %)	0.12 (37 %)
2	USA	0.14 (64 %)	0.13 (61 %)	0.14 (54 %)	0.11 (53 %)
3	CAM	0.09 (52 %)	0.09 (50 %)	0.10 (49 %)	0.08 (43 %)
4	EUR	0.30 (69 %)	0.24 (62 %)	0.20 (46 %)	0.17 (42 %)
5	RUS	0.25 (59 %)	0.24 (60 %)	0.21 (42 %)	0.20 (42 %)
6	CAS	0.35 (30 %)	0.36 (30 %)	0.38 (20 %)	0.37 (19 %)
7	EAS	0.24 (45 %)	0.25 (50 %)	0.27 (47 %)	0.28 (53 %)
8	SAS	0.24 (21 %)	0.26 (27 %)	0.29 (31 %)	0.26 (43 %)
9	SEA	0.09 (51 %)	0.10 (49 %)	0.09 (49 %)	0.11 (65 %)
10	SHR	0.46 (11 %)	0.46 (11 %)	0.44 (9 %)	0.44 (8 %)
11	SHL	0.52 (10 %)	0.62 (9 %)	0.61 (8 %)	0.55 (9 %)
12	MDE	0.36 (17 %)	0.35 (19 %)	0.38 (20 %)	0.37 (19 %)
13	SAM	0.07 (52 %)	0.08 (42 %)	0.07 (33 %)	0.06 (42 %)
14	RAF	0.18 (40 %)	0.20 (37 %)	0.22 (32 %)	0.17 (39 %)
15	ANZ	0.07 (27 %)	0.08 (24 %)	0.07 (29 %)	0.06 (28 %)
Ocean regions:					
1	NAT	0.17 (48 %)	0.16 (43 %)	0.15 (35 %)	0.13 (32 %)
2	WNP	0.20 (36 %)	0.20 (41 %)	0.22 (35 %)	0.23 (40 %)
3	ENP	0.14 (24 %)	0.13 (27 %)	0.15 (24 %)	0.15 (29 %)
4	CAT	0.15 (24 %)	0.18 (21 %)	0.17 (19 %)	0.14 (21 %)
5	WCP	0.06 (38 %)	0.07 (38 %)	0.07 (33 %)	0.07 (46 %)
6	ECP	0.06 (27 %)	0.07 (26 %)	0.07 (23 %)	0.06 (24 %)
7	NIN	0.16 (23 %)	0.17 (24 %)	0.16 (33 %)	0.17 (38 %)
8	WSP	0.04 (24 %)	0.06 (18 %)	0.06 (17 %)	0.05 (22 %)
9	ESP	0.04 (21 %)	0.05 (17 %)	0.05 (11 %)	0.04 (16 %)
10	SIN	0.05 (24 %)	0.07 (22 %)	0.06 (19 %)	0.05 (27 %)
11	SAT	0.07 (44 %)	0.08 (39 %)	0.08 (31 %)	0.06 (36 %)
12	SOU	0.08 (9 %)	0.10 (8 %)	0.10 (6 %)	0.08 (8 %)
Polar regions:					
Arctic		0.17 (52 %)	0.17 (53 %)	0.14 (32 %)	0.11 (34 %)
Antarctic		0.03 (15 %)	0.06 (8 %)	0.09 (5 %)	0.04 (13 %)
Global:					
Land		0.19 (38 %)	0.20 (37 %)	0.20 (30 %)	0.18 (33 %)
Ocean		0.09 (31 %)	0.10 (28 %)	0.10 (23 %)	0.09 (27 %)
Land + ocean		0.12 (34 %)	0.13 (32 %)	0.13 (26 %)	0.11 (29 %)

ACPD
13, 19751–19835, 2013

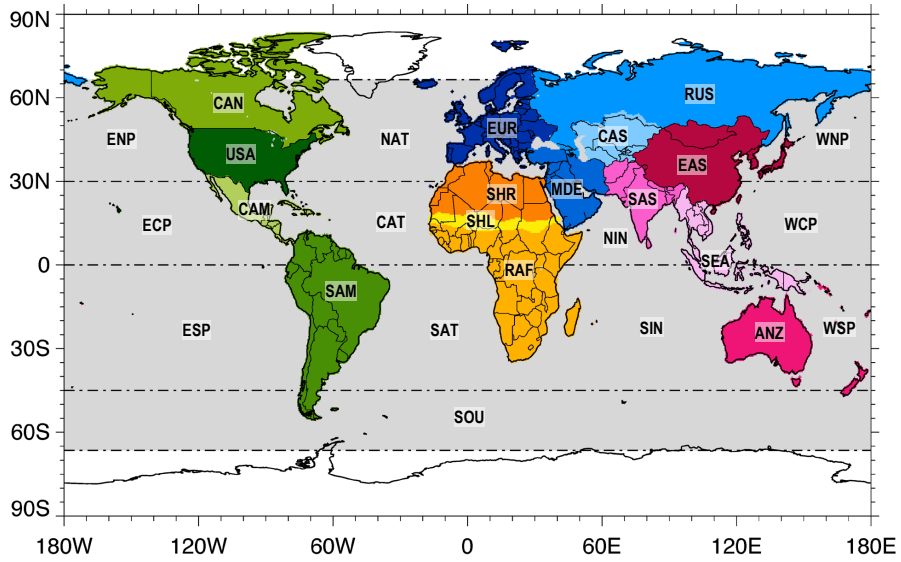

Fig. 1. Land and ocean region domains defined in this study. Region description, abbreviation, and surface area listed in Table 1.

ACPD
13, 19751–19835, 2013

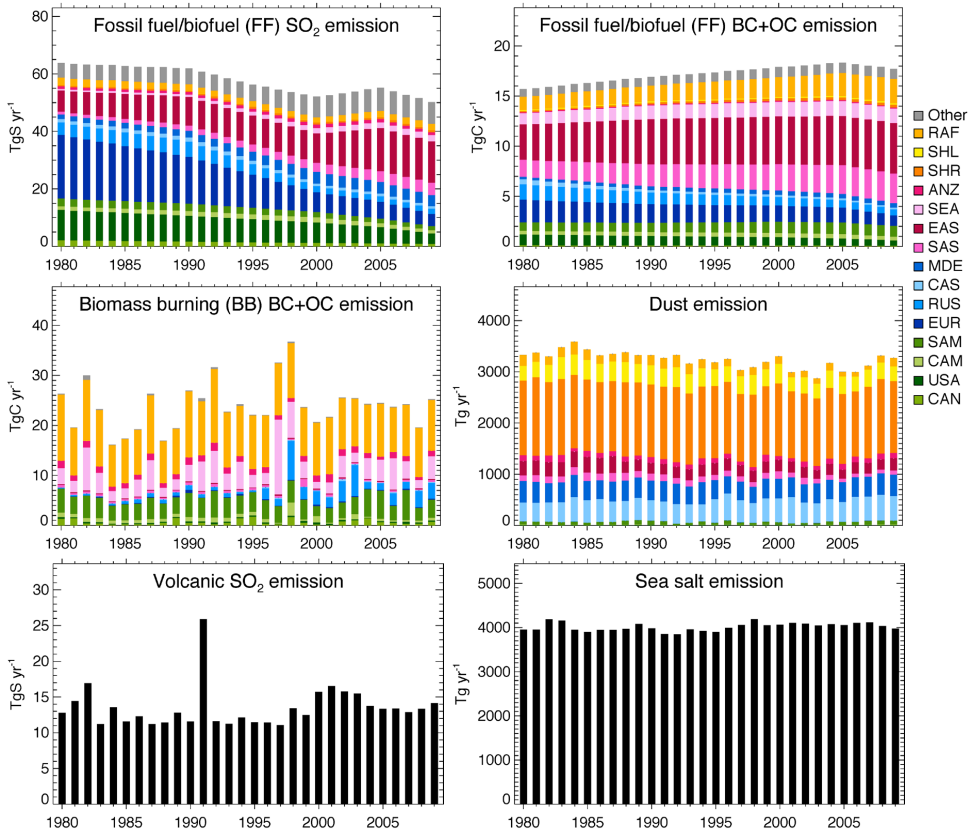

Fig. 2a. Global and regional annual total emissions of fossil fuel/biofuel (FF) SO_2 (top left) and BC + OC (top right), biomass burning (BB) BC + OC (middle left), dust (middle right), volcanic SO_2 (bottom left), and sea salt (bottom right) from 1980 to 2009 used in this work. Region domains and corresponding color shades are shown in Fig. 1.

ACPD
13, 19751–19835, 2013

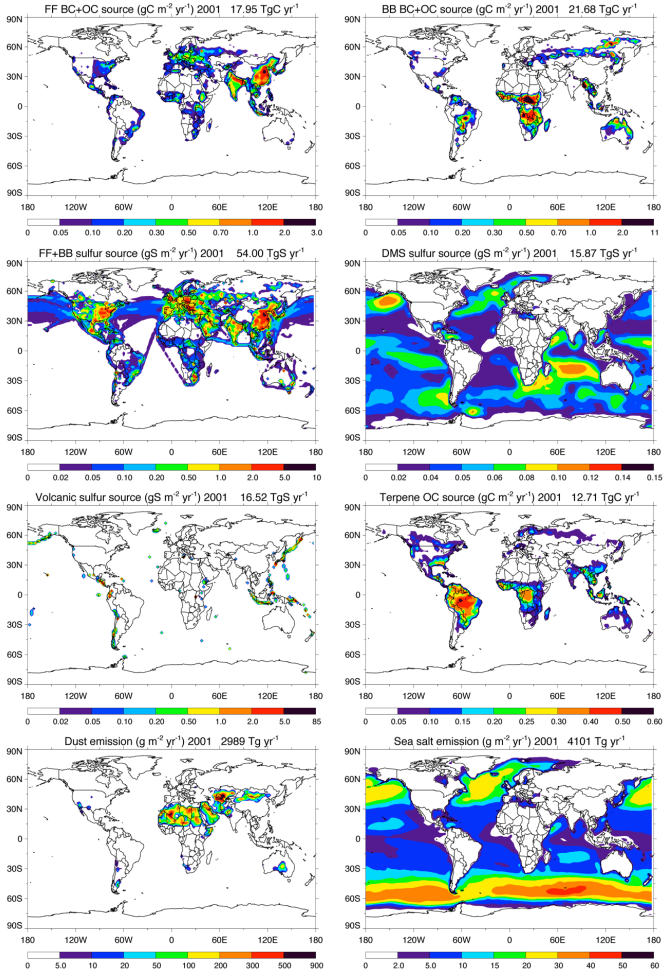

ACPD
13, 19751–19835, 2013

Sources and regional trends

Mian Chin et al.

Fig. 2b. Global sources of fossil fuel/biofuel (FF) OC + BC (top left), biomass burning (BB) OC + BC (top right), FF + BB SO_2+sulfate (2nd row left), DMS (2nd row right), volcanic SO_2 (3rd row left), biogenic OC (3rd row right), dust (bottom left), and sea salt (bottom right) in 2001. The latter five are considered as natural sources. See text for more details.

ACPD
13, 19751–19835, 2013

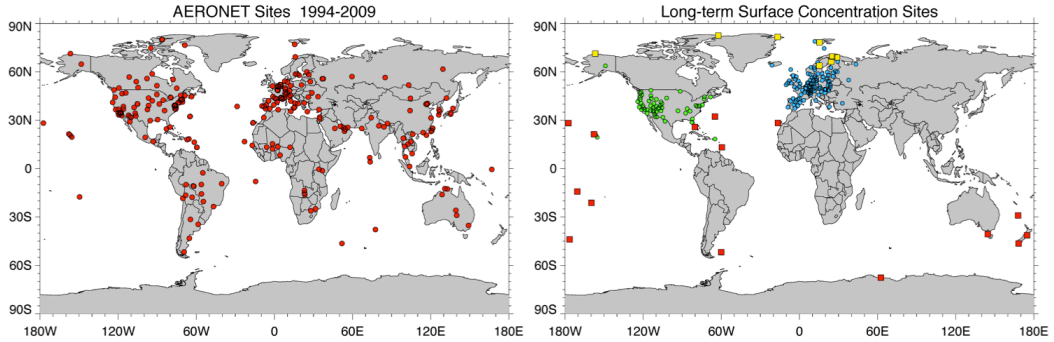

Fig. 3. Locations of AERONET sunphotometer sites (left) and surface concentration sites (right) of IMPROVE network in the US (green circles), EMEP network in Europe (blue circles), University of Miami sites on the ocean islands (red squares), and Arctic sites (yellow squares).

ACPD
13, 19751–19835, 2013

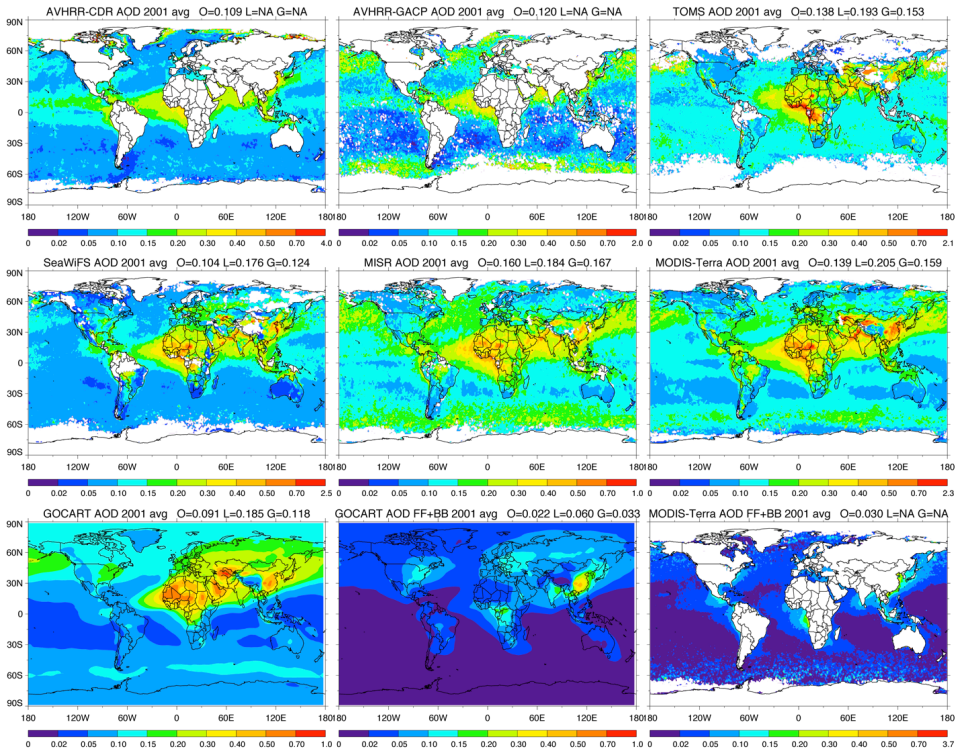

Fig. 4. Spatial distributions of 2001 annual average AOD from satellite retrieval products and GOCART model. From left to right, 1st row: AVHRR-CDR, AVHRR-GACP, TOMS; 2nd row: SeaWiFS, MISR, MODIS-Terra; 3rd row: GOCART total AOD, GOCART FF + BB AOD, and MODIS-derived FF + BB AOD. White area indicating no data. Annual average values over ocean (O), land (L), and globe (G) are indicated on top of each panel (NA = not available). These averages are obtained with the available data from each individual dataset without matching their spatial availability, i.e., the area included in the average varies with datasets.

ACPD
13, 19751–19835, 2013

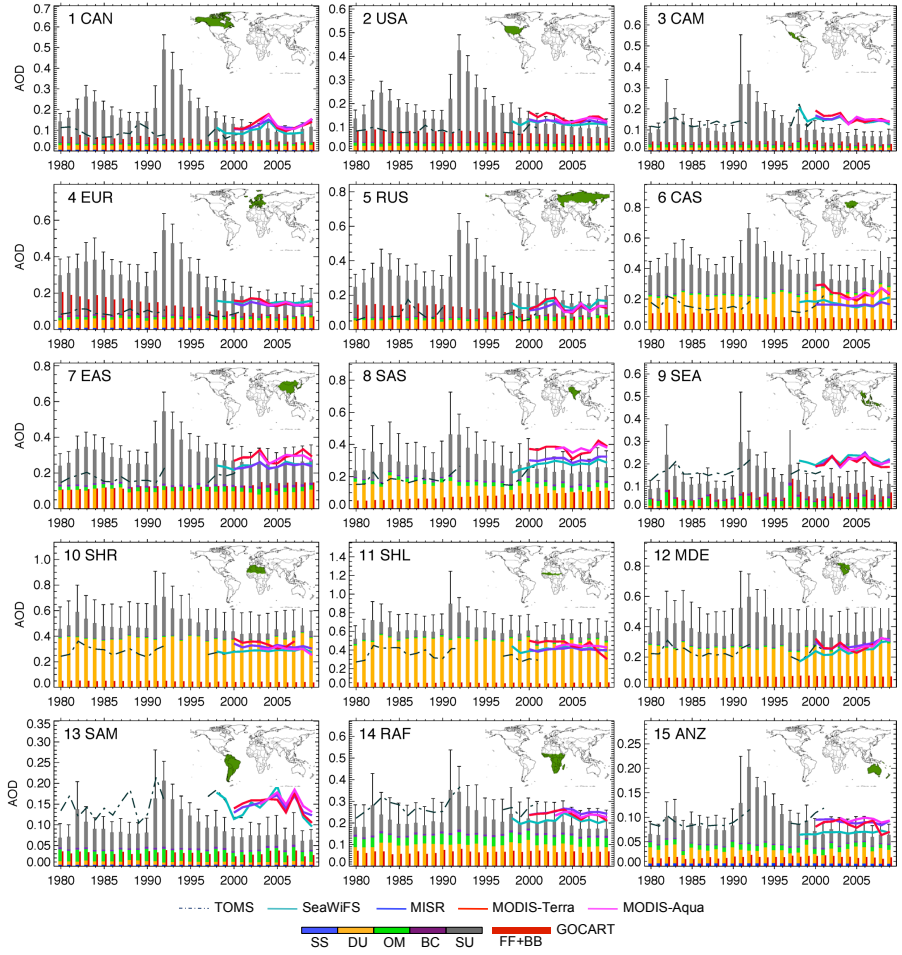

ACPD
13, 19751–19835, 2013

Sources and regional trends

Mian Chin et al.

Fig. 5a. Regional annual average AOD from 1980 to 2009 in 15 land regions. Region domains are shown in Fig. 1 and also shaded in green on each panel, with names and surface areas listed in Table 1. Satellite retrievals are presented in continuous color lines, and GOCART results are displayed in vertically stacked color bars showing AOD composition (SS = sea salt, DU = dust, OM = organic matter, BC = black carbon, and SU = sulfate). AOD from fossil fuel and biomass burning (FF + BB) sources is shown in red vertical lines next to the aerosol composition. All products are averaged within the region domains without considering coincidental spatial/temporal coverage. Note that there is no AVHRR retrieval available over land. Standard deviation of monthly average of regional AOD from GOCART is shown in thin black vertical lines (for clarity, only positive part is plotted and the deviation from satellite data is not displayed).

ACPD
13, 19751–19835, 2013

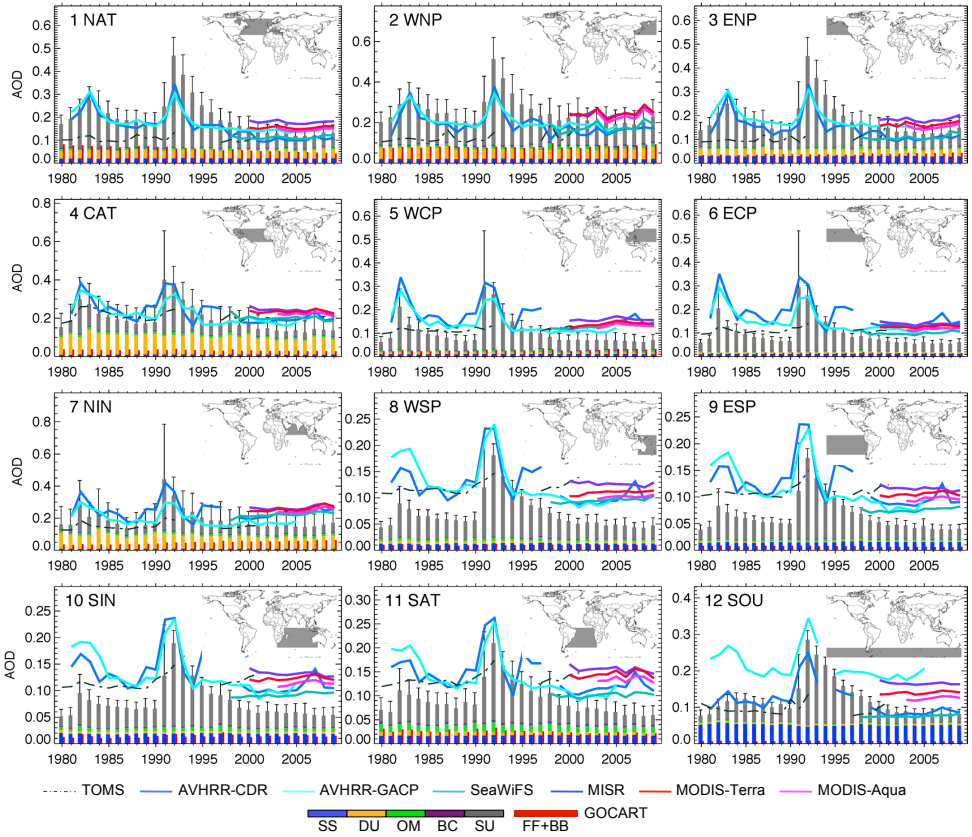

Fig. 5b. Same as **(a)** but for 12 ocean regions (domains shaded in grey) with AVHRR retrievals available.

ACPD
13, 19751–19835, 2013

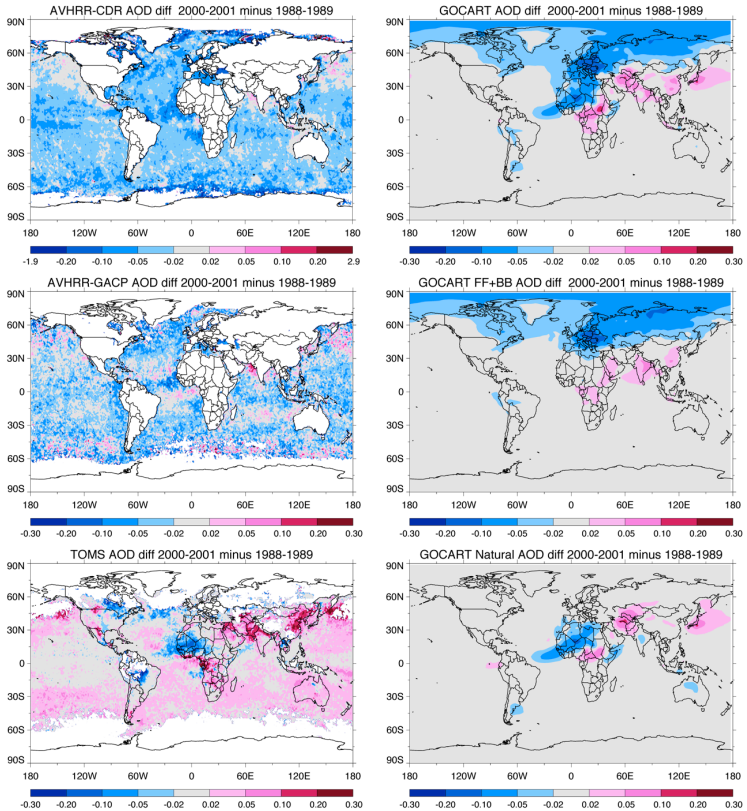

Fig. 6a. Difference of AOD between 2000–2001 and 1988–1989 from satellite data (left colum, from top: AVHRR-CDR, AVHRR-GACP, and TOMS) and GOCART simulations (right column, from top: total, FF + BB, and natural AOD). White area indicating no data.

ACPD
13, 19751–19835, 2013

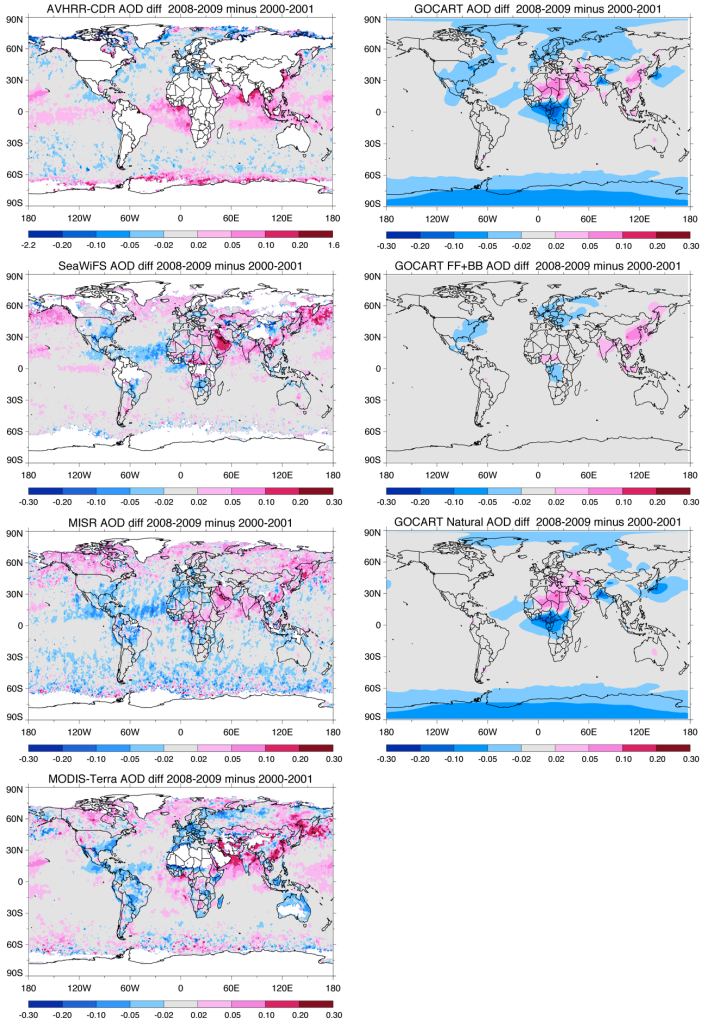

ACPD
13, 19751–19835, 2013

Sources and regional trends

Mian Chin et al.

Fig. 6b. Difference of AOD between 2008–2009 and 2000–2001 from satellite data (left column, from top: AVHRR-CDR, SeaWiFS, MISR, and MODIS-Terra) and GOCART simulations (right column, from top: total, FF + BB, and natural AOD). White area indicating no data. The data gap over the desert regions in MODIS-Terra is due to the unavailability of Deep Blue products in 2008 and 2009.

ACPD
13, 19751–19835, 2013

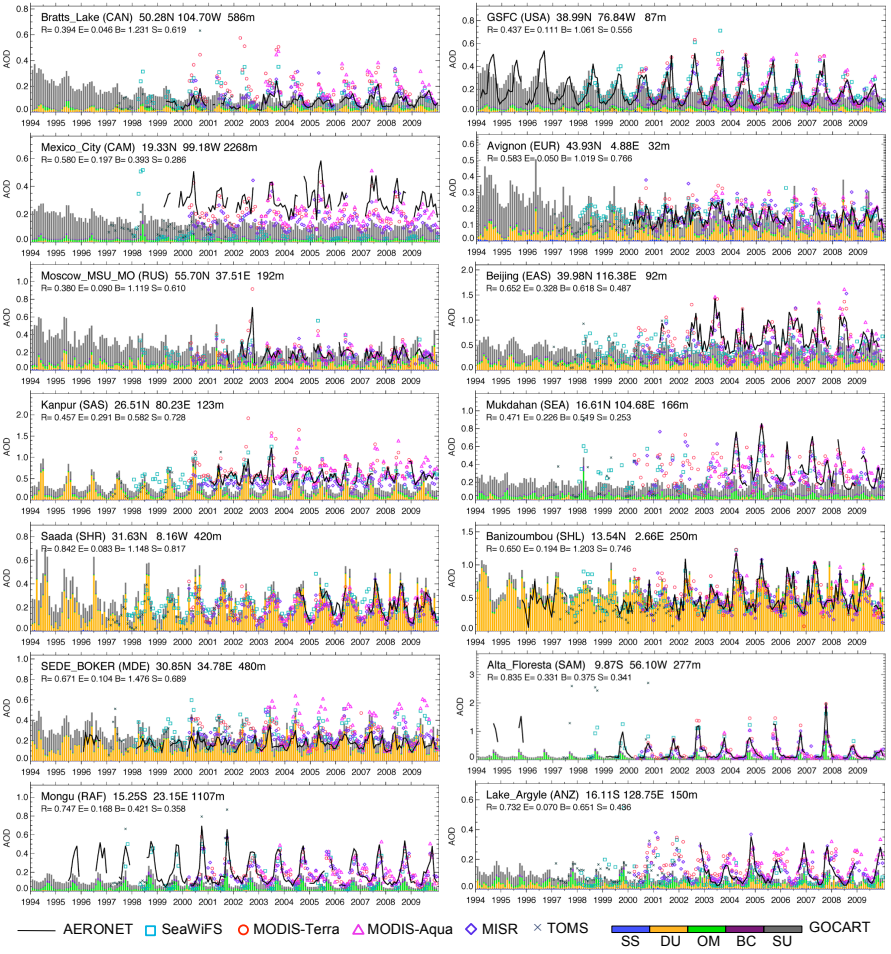

ACPD
13, 19751–19835, 2013

Sources and regional trends

Mian Chin et al.

Fig. 7a. AOD at AERONET sites in 14 land regions (region name in parenthesis and domain in Fig. 1) from 1994 to 2009 (shown 1 site each region; no AERONET long-term data over CAS region). AERONET data are in black lines, satellite data are in color symbols, and GOCART results are displayed in vertically stacked color lines showing AOD composition (SS = sea salt, DU = dust, OM = organic matter, BC = black carbon, and SU = sulfate). Statistical measures of comparisons between AERONET and GOCART are shown on each panel: R = correlation coefficient, E = root-mean-square-error, B = mean bias (model/observation), and S = skill score (Taylor, 2001).

ACPD
13, 19751–19835, 2013

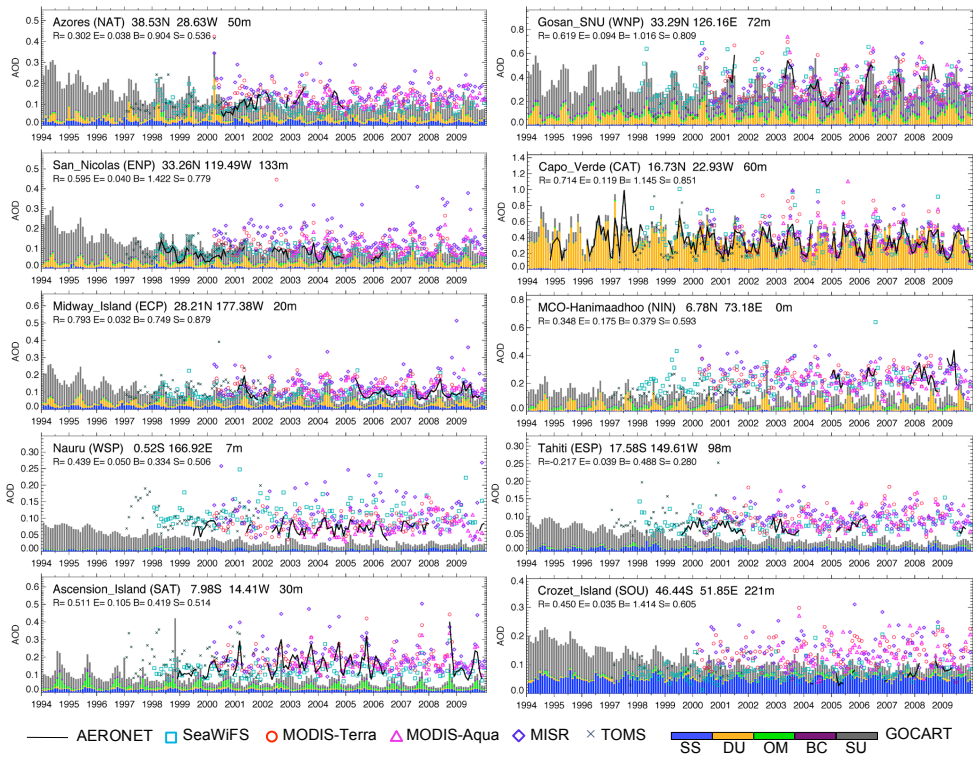

Fig. 7b. Same as **(a)** but for 10 oceanic island sites (shown 1 site for each oceanic region, except no long-term sites in SIN and WCP).

ACPD
13, 19751–19835, 2013

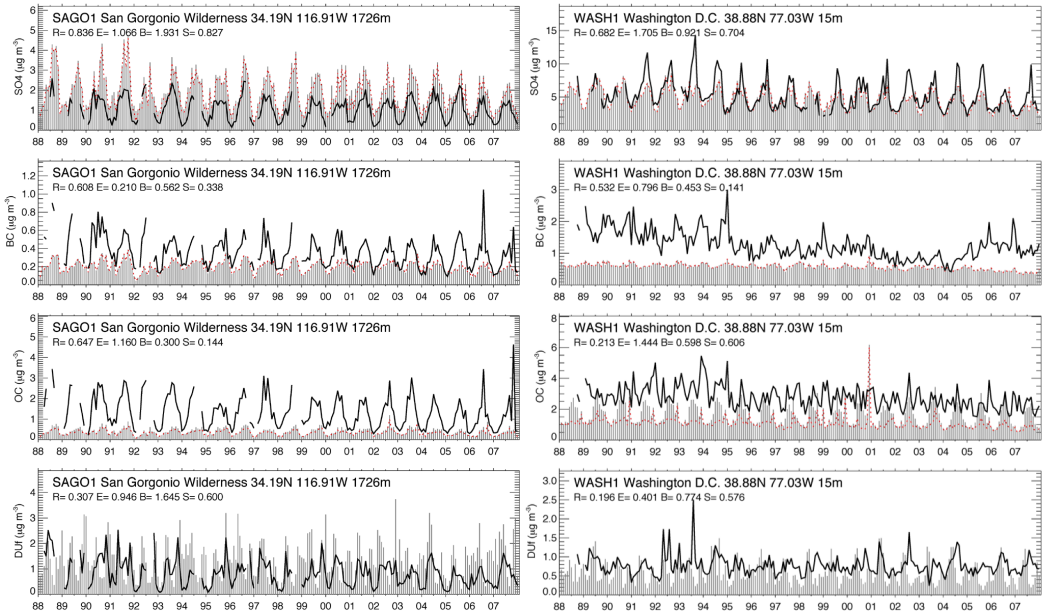

Fig. 8a. Monthly averaged surface concentrations ($\mu g\,m^{-3}$) of sulfate (top row), BC (2nd row), OC (3rd row), and fine mode dust (bottom row) from 1988 to 2007 at two US sites, San Gorgonio Wilderness in California, Western US (left column) and Washington DC, Eastern US (right column) from the IMPROVE network. Observations are shown in black lines and the model results in grey bars for total amount and dotted red lines for FF + BB amount. Statistical measures (R, E, B, and S) are defined as the same as in Fig. 7a caption.

ACPD
13, 19751–19835, 2013

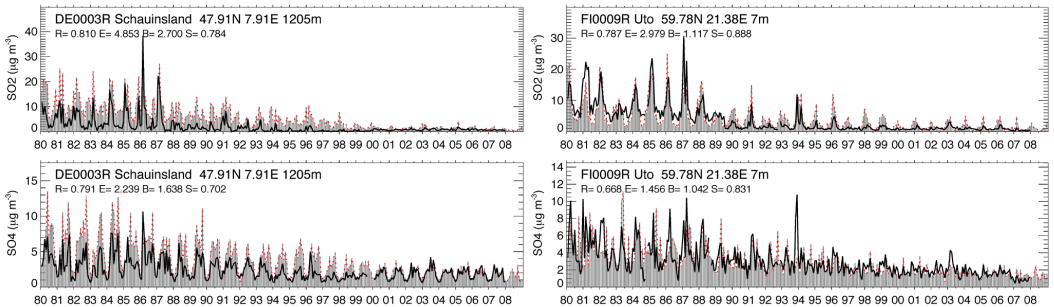

Fig. 8b. Monthly averaged surface SO_2 (top row) and sulfate (bottom row) concentrations ($\mu g\,m^{-3}$) from 1980 to 2008 at two European sites, Schauinsland, Germany (left column) and Uto in Finland (right column), in the EMEP network. Observations are shown in black lines and the model results in grey bars for total amount and dotted red lines for FF + BB amount. Statistical measures (R, E, B, and S) are defined as the same as in Fig. 7a caption.

ACPD
13, 19751–19835, 2013

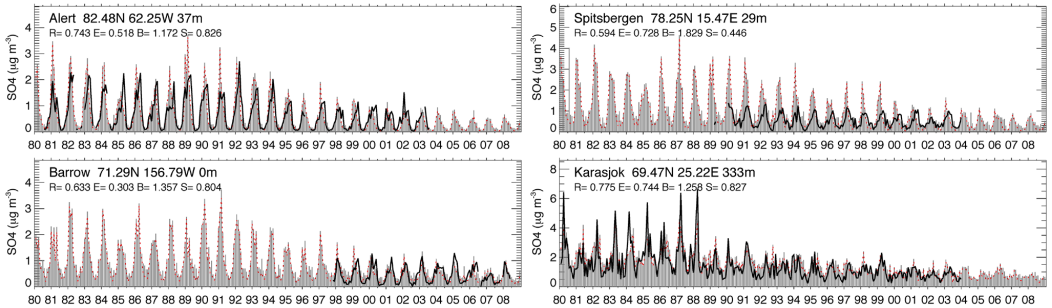

Fig. 8c. Monthly averaged surface sulfate concentrations ($\mu g\,m^{-3}$) from 1980 to 2008 at four Arctic sites, two in the Western Arctic (left column) and two in the Eastern Arctic (right row). Observations are shown in black lines and the model results in grey bars for total amount and dotted red lines for FF + BB amount. Statistical measures (R, E, B, and S) are defined as the same as in Fig. 7a caption.

ACPD
13, 19751–19835, 2013

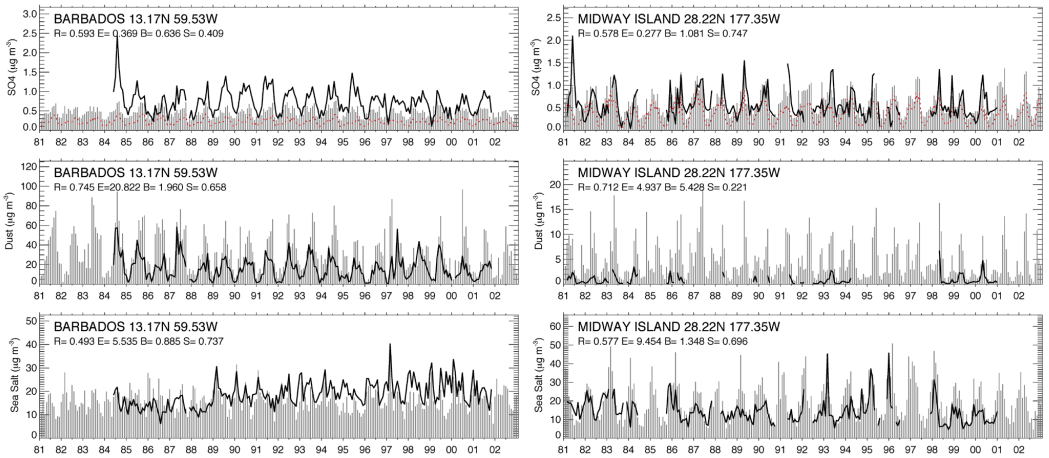

Fig. 8d. Monthly averaged surface concentrations ($\mu g\,m^{-3}$) of non-sea-salt sulfate (top row), dust (2nd row), and sea salt (3rd row), from 1981 to 2002 at Barbados in North Atlantic (left column) and Midway Island in North Pacific (right column) from the University of Miami network. Observations are shown in black lines and the model results in grey bars for total amount and dotted red lines for FF + BB amount. Statistical measures (R, E, B, and S) are defined as the same as in Fig. 7a caption.

ACPD
13, 19751–19835, 2013

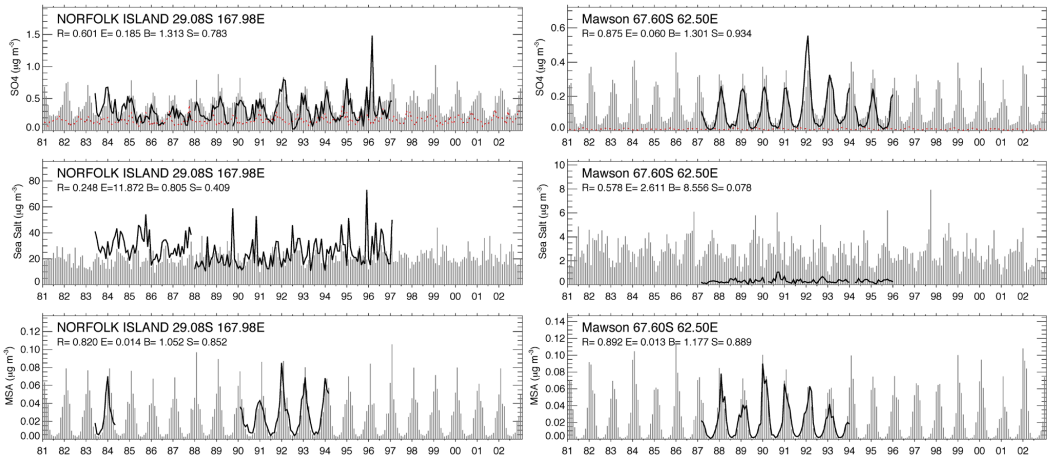

Fig. 8e. Monthly averaged surface concentrations ($\mu g\,m^{-3}$) of non-sea-salt sulfate (top row), sea salt (2nd row), and MSA (3rd row), from 1981 to 2002 at Norfolk Island in South Pacific (left column) and Mawson Station off the coast of Antarctic (right column) from the University of Miami network. Observations are shown in black lines and the model results in grey bars for total amount and dotted red lines for FF + BB amount. Statistical measures (R, E, B, and S) are defined as the same as in Fig. 7a caption.

ACPD
13, 19751–19835, 2013

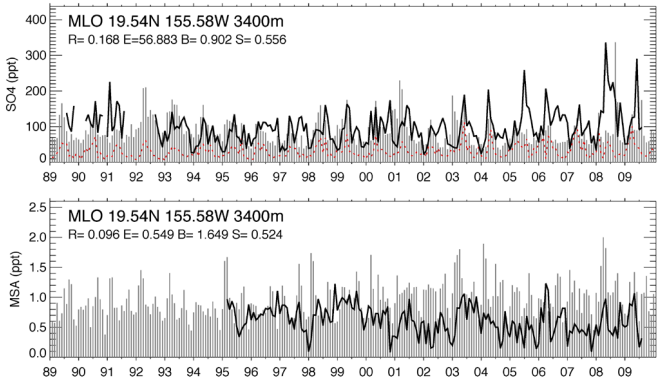

Fig. 8f. Monthly averaged concentrations (ppt by moles) of non-sea-salt sulfate (top row) and MSA (bottom row) from 1989 to 2009 at the Mauna Loa Observatory from the University of Hawaii. Observations are shown in black lines and the model results in grey bars for total amount and dotted red lines for FF + BB amount. Statistical measures (R, E, B, and S) are defined as the same as in Fig. 7a caption.

ACPD
13, 19751–19835, 2013

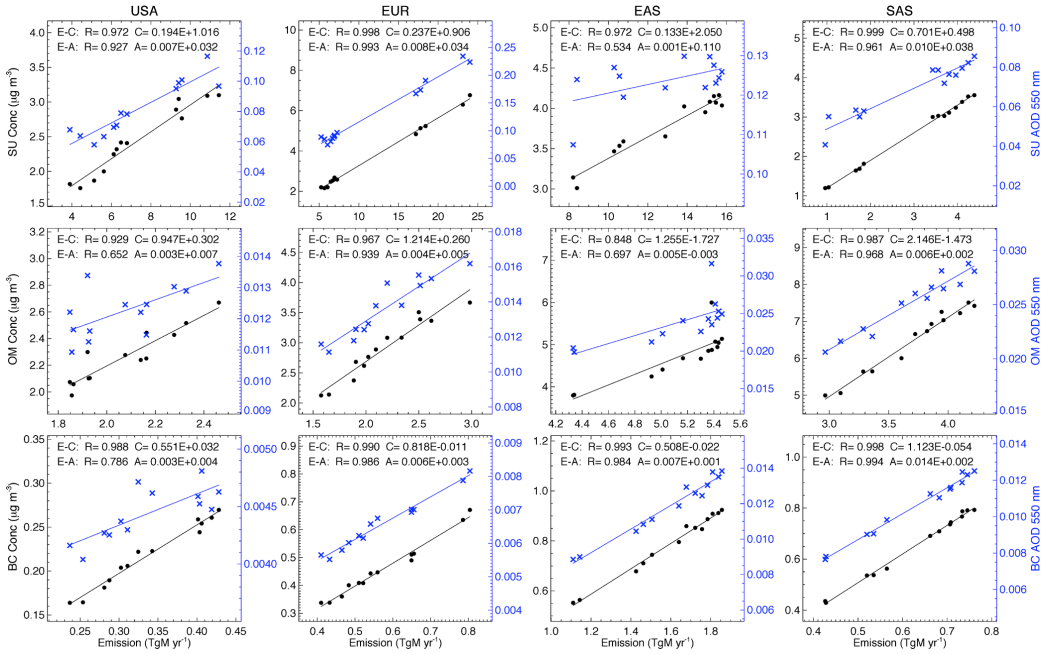

Fig. 9. Model estimated relationship between emission (E) and surface concentrations (C) (black dots) or AOD (A) (blue crosses) of sulfur (total sulfur emissions, mainly SO_2, and sulfate concentration or AOD) (1st row), OM (2nd row), and BC (3rd row) on regional and annual average over USA (1st column), Europe (2nd column), East Asia (3rd column), and South Asia (4th column) in years without large scale volcanic influence (1980–1981, 1988–1990, and 2002–2009). Emissions are expressed as annual total within the individual regions in Tg M yr^{-1}, where M is S for sulfur and C for BC and OM.

ACPD
13, 19751–19835, 2013

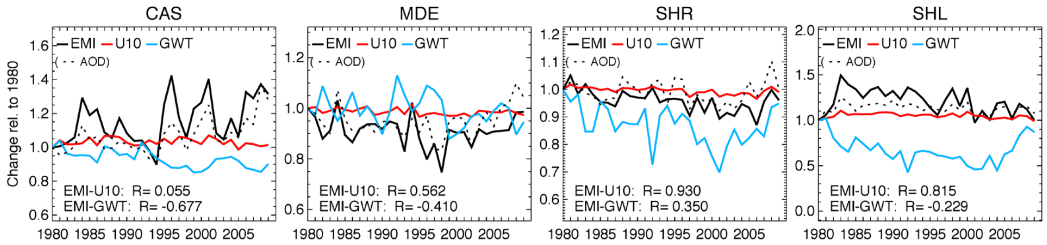

Fig. 10. Regional and annual averaged changes of GOCART dust emission (EMI, black line) and its controlling parameters of 10 m wind speed (U10, red line) and ground wetness (GWT, blue line) from MERRA from 1980 to 2009 relative to their 1980 values in dust source regions. (Superimposed dotted line is the corresponding dust AOD). Note the linear correlation coefficients on regional and annual average scale do not represent the relationship between emission and the meteorological parameters shown in Eq. (1); here they just serve as indicators on the relative closeness between the emission and meteorological parameters. Also note that the magnitude of the relative change of wind speed is much smaller than that of other variables on such large spatial and temporal averaged scales.

ACPD
13, 19751–19835, 2013

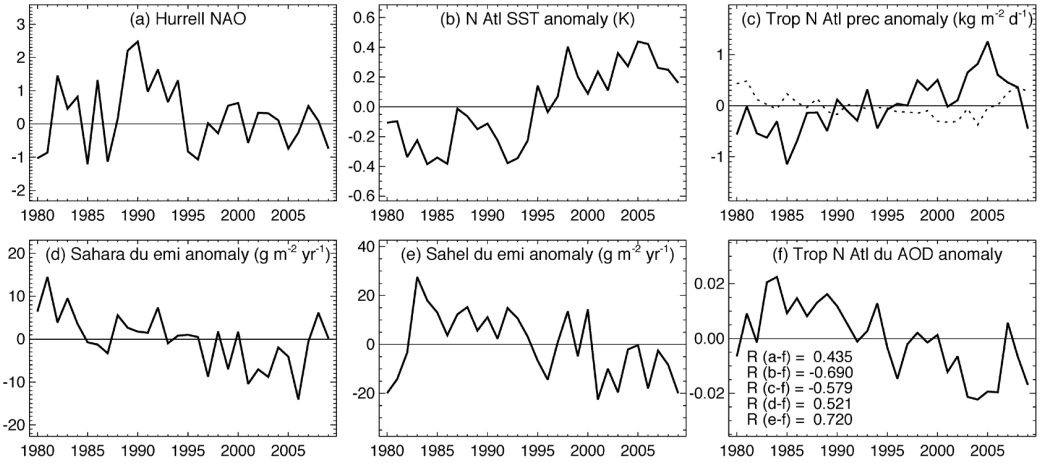

Fig. 11. Time series of **(a)** Hurrell principle component-based NAO index (http://climatedataguide.ucar.edu/guidance/hurrell-north-atlantic-oscillation-nao-index-pc-based), anomalies of MERRA reanalysis of **(b)** North Atlantic SST (0–66° N) and **(c)** precipitation in tropical North Atlantic (5° N–20° N, 90° W–18° W), and anomalies of GOCART calculated **(d)** dust emissions in Sahara and **(e)** Sahel and **(f)** dust AOD over tropical North Atlantic ocean. The correlation coefficients of the dust AOD anomaly over the tropical North Atlantic with other quantities in **(a)–(e)** are shown in the last panel. Superimposed in panel **(c)** in dotted line is the precipitation anomaly in Sahel.

ACPD
13, 19751–19835, 2013